

# Dark matter content and internal dynamics of NGC 4697: NMAGIC particle models from slit data and planetary nebulae velocities

Flavio De Lorenzi<sup>1,2\*</sup>, Ortwin Gerhard<sup>1</sup>, Roberto P. Saglia<sup>1</sup>, Niranjan Sambhus<sup>2</sup>

Victor P. Debattista<sup>3†</sup>, Maurilio Pannella<sup>1</sup>, Roberto H. Méndez<sup>4</sup>

<sup>1</sup> *Max-Planck-Institut für Ex. Physik, Giessenbachstraße, D-85741 Garching, Germany*

<sup>2</sup> *Astron. Institut, Universität Basel, Venusstrasse 7, Binningen, CH-4102, Switzerland*

<sup>3</sup> *Centre for Astrophysics, University of Central Lancashire, Preston, PR1 2HE, UK*

<sup>4</sup> *Institute for Astronomy, University of Hawaii, 2680 Woodlawn Drive, Honolulu, HI 96822, USA*

Accepted —. Received —; in original form —

## ABSTRACT

We present a dynamical study of NGC 4697, an almost edge-on, intermediate-luminosity, E4 elliptical galaxy, combining new surface brightness photometry, new as well as published long-slit absorption line kinematic data, and published planetary nebulae (PNe) velocity data. The combined kinematic data set extends out to  $\simeq 5' \simeq 4.5R_e$  and allows us to probe the galaxy's outer halo.

For the first time, we model such a dataset with the new and flexible  $\chi^2$ -made-to-measure particle code NMAGIC. We extend NMAGIC to include seeing effects, introduce an efficient scheme to estimate the mass-to-light ratio, and incorporate a maximum likelihood technique to account for discrete velocity measurements.

For modelling the PNe kinematics we use line-of-sight velocities and velocity dispersions computed on two different spatial grids, and we also use the individual velocity measurements with the likelihood method, in order to make sure that our results are not biased by the way we treat the PNe measurements.

We generate axisymmetric self-consistent models as well models including various dark matter halos. These models fit all the mean velocity and velocity dispersion data with  $\chi^2/N < 1$ , both in the case with only luminous matter and in potentials including quite massive halos. The likelihood analysis together with the velocity histograms suggest that models with low density halos such that the circular velocity  $v_c \lesssim 200 \text{ km s}^{-1}$  at  $5R_e$  are not consistent with the data. A range of massive halos with  $v_c \simeq 250 \text{ km s}^{-1}$  at  $5R_e$  fit the PN data best. To derive stronger results would require PN velocities at even larger radii. The best fitting models are slightly radially anisotropic; the anisotropy parameter  $\beta \simeq 0.3$  at the center, increasing to  $\beta \simeq 0.5$  at radii  $\gtrsim 2R_e$ .

**Key words:** galaxies: kinematics and dynamics – galaxies: elliptical and lenticular, cD – galaxies: individual: NGC 4697 – galaxies: halos – cosmology: dark matter – methods:  $N$ -body simulation

## 1 INTRODUCTION

The presence of dark matter (DM) has long been inferred around spiral galaxies from their flat rotation curves, and galaxies are now generally believed to be surrounded by extended dark matter halos. Indeed, in the current  $\Lambda$ -cold dark

matter ( $\Lambda$ CDM) cosmology, galaxies form within the potential wells of their halos. The standard picture for the formation of elliptical galaxies is through mergers of smaller units. Ellipticals should thus also be surrounded by dark matter halos. Their halos are particularly interesting because ellipticals are among the oldest galaxies and are found in the densest environments.

Unfortunately, mass measurements in elliptical galaxies have been difficult because of the lack of a suit-

\* E-mail: lorenzi@mpe.mpg.de

† RCUK Academic Fellow

able ubiquitous tracer such as neutral hydrogen rotation curves in spirals. In giant ellipticals, there is evidence for dark matter from X-ray emission (*e.g.* Awaki et al. 1994; Loewenstein & White 1999; Humphrey et al. 2006) and gravitational lensing (*e.g.* Griffiths et al. 1996; Treu & Koopmans 2004; Rusin & Kochanek 2005). In more ordinary ellipticals, mass estimates come from stellar dynamical studies, which have been limited by the faintness of the galaxies' outer surface brightness to radii less than two effective radii from the centre,  $R \lesssim 2R_e$  (*e.g.* Kronawitter et al. 2000; Thomas et al. 2007). These studies suggest that the dark matter contributes  $\sim 10 - 40\%$  of the mass within  $R_e$  (Gerhard et al. 2001; Cappellari et al. 2006), consistent with the lensing results.

The strong emission line at [OIII] $\lambda$ 5007 from planetary nebulae offers a promising tool to overcome this limitation and to extend stellar kinematic studies to larger radii (Hui et al. 1995; Tremblay et al. 1995; Arnaboldi et al. 1996, 1998). Also, in the less massive, X-ray faint ellipticals, PNe may be the primary tool for constraining the dynamics at large radii. Once the PNe are identified, their line-of-sight velocities can be obtained from the Doppler shift of the narrow emission line. Interestingly, the derived PNe dispersion profiles in the elliptical galaxies NGC 4697 (Méndez et al. 2001) and NGC 821, 3379 and 4494 (Romanowsky et al. 2003; Douglas et al. 2007) were found to decline significantly with radius outside  $1R_e$ . Their spherically symmetric dynamical analysis led Romanowsky et al. (2003) to the conclusion that these galaxies lack massive dark matter halos; however, Dekel et al. (2005) argued that the well known mass-anisotropy degeneracy allows for declining dispersion profiles even when a standard DM halo is present.

In the present paper we focus on NGC 4697, a normal and almost edge-on E4 galaxy located along the Virgo southern extension. Méndez et al. (2001) obtained a planetary nebula luminosity function (PNLF) distance of  $10.5 \pm 1$  Mpc from magnitudes of 531 PNe, and Tonry et al. (2001) measured a surface brightness fluctuation (SBF) distance of  $11.7 \pm 0.1$  Mpc. This fairly isolated galaxy has a total B magnitude  $B_T = 10.14$  and harbors a central super massive black hole (SMBH) of mass  $1.2 \times 10^8 M_\odot$  (Pinkney et al. 2000). A Sersic law with  $R_e = 66$  arcsec gives a good fit to the surface brightness profile out to about 4 arcmin (see Section 2). Based on the disk isophote shapes Carter (1987) and Goudfrooij et al. (1994) inferred a stellar disk along the major axis. The contribution of the disk kinematics to the major axis line-of-sight velocity distributions was estimated by Scorza et al. (1998). X-ray observations with ROSAT (Sansom et al. 2000) show a lack of large scale hot gas in the halo of this galaxy. Using more recent Chandra data, Irwin et al. (2000) could resolve most of this emission into non-uniformly distributed low mass X-ray binary (LMXB) point sources, suggesting that NGC 4697 is mostly devoid of interstellar gas and perhaps does not have substantial amounts of DM.

Dynamical models of NGC 4697 have been constructed by Binney et al. (1990) and Dejonghe et al. (1996), both based on photometry and absorption line kinematic data within  $\sim 1R_e$ . The data were consistent with a constant mass-to-light-ratio and none of these models showed evidence for dark matter. Méndez et al. (2001) obtained velocities for 531 PNe and derived a velocity dispersion profile out

to approximately  $4.5R_e$ . Assuming an isotropic velocity distribution, Méndez et al. (2001) found that the PNe velocity dispersion profile is consistent with no DM inside  $4.5R_e$ , but that DM can be present if the velocity distribution is anisotropic. This was also argued by Dekel et al. (2005) to be the main cause of the finding by Romanowsky et al. (2003), that their three intermediate luminosity galaxies lacked significant dark matter halos (but see Douglas et al. 2007). Contrary to these three galaxies, which are nearly round on the sky, NGC 4697 is strongly flattened and likely to be nearly edge-on, thus easier to model since shape degeneracies are much less severe.

In the light of this, it is important enough to perform a further careful analysis of this galaxy. In this paper we construct dynamical models of NGC 4697 with the very flexible NMAGIC particle code, making use of new and published slit kinematics and the Méndez et al. (2001) PN data. The paper is organized as follows. In Section 2 we describe our new observational data and all other data that are used for the dynamical models. In Section 3 we give a brief explanation of the NMAGIC modeling technique. We extend the method to include seeing effects, introduce an efficient scheme to estimate the mass-to-light ratio, and show how discrete velocity measurements may be taken into account. In Section 4 we construct isotropic rotator models to test and calibrate the method, preparing for the dynamical modeling of NGC 4697 which is then performed in Section 5. Finally, the paper closes with our conclusions in Section 6.

## 2 OBSERVATIONAL DATA

In this section, we describe the observational data used in the present study, including new CCD photometry and new long-slit absorption line kinematics. We also describe here the procedure employed for the deprojection of the photometric data. In the following we adopt a distance 10.5 Mpc to NGC 4697 (Méndez et al. 2001).

### 2.1 Surface Photometry

The R-band data used in the present work were taken in April 2000 as part of the ESO Proposal 064.N-0030 (P.I. R.P. Saglia) at the Wide Field Imager on the ESO-MPIA 2.2m telescope. Six 5 minutes, dithered exposures were taken in sub-arcsec seeing conditions. After the usual data reduction procedures (performed using the IRAF task *mscred*), the data were tabulated as radial profiles of surface brightness  $\mu$ , ellipticity  $\epsilon$ , position angle PA and Fourier shape coefficients (Bender & Moellenhoff 1987). The surface brightness was calibrated using the R band photometry of Peletier et al. (1990). Systematic errors due to sky subtraction ( $\mu_{sky} = 20.18$  Rmag arcsec $^{-2}$ ) are always smaller than 10%. Fig. A1 shows the derived profiles and Table A gives them in tabular form. The isophotes of NGC 4697 do not show any appreciable twist in PA and have a positive  $a_4$  coefficient in the galaxy's inner parts, which is well-explained by a near-edge-on embedded disk (Scorza & Bender 1995). The galaxy has some dust in the inner regions (Pinkney et al. 2003), but the R-band observations are relatively unaffected by it. The outer isophotes are progressively slightly off-centered. A Sersic fit to the surface brightness profile results in Sersic

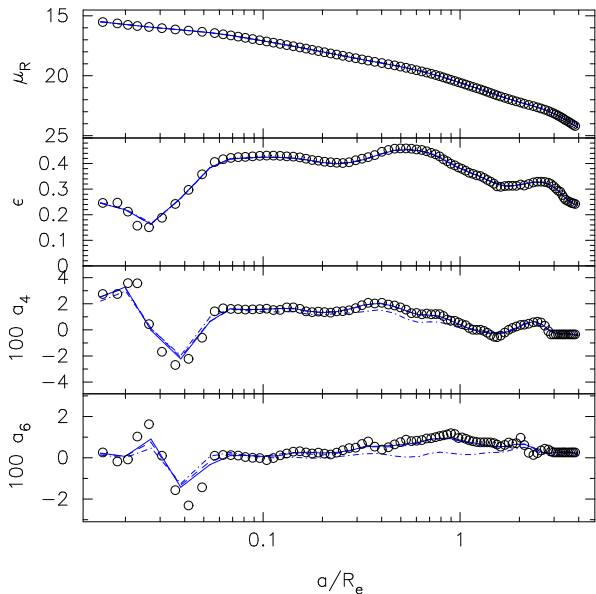


**Figure 1.** Comparison of the photometry of NGC 4697 with reprojected three-dimensional luminosity models. The data points correspond to the observed photometry for NGC 4697 (for the deprojection, the  $a_4$  and  $a_6$  values have been set to constants beyond  $\simeq 3R_e$ ). The solid line shows the edge-on deprojected model reprojected, the dashed line the  $i = 80^\circ$  deprojected model reprojected, and the dash-dotted line the  $i = 67^\circ$  model. The panels show, from top to bottom, surface brightness  $\mu_R$ , ellipticity  $\epsilon$  and the isophotal shape parameters  $a_4$  and  $a_6$ .

index  $n = 3.5$  and effective radius  $R_e = 66$  arcsec. The older value of 95 arcsec from Binney et al. (1990) was based on photometry reaching only 120 arcsec; thus we use  $R_e = 66$  arcsec in the following. For a distance of 10.5 Mpc this corresponds to 3.36 kpc.

## 2.2 Deprojection

For our dynamical study, we will fit particle models to the deprojected luminosity density using NMAGIC, *cf.* Section 3. To obtain the luminosity density we need to deproject the surface brightness. This inversion problem is unique only for spherical or edge-on axisymmetric systems (Binney & Tremaine 1987). For axisymmetric systems inclined at an angle  $i$ , the Fourier slice theorem (Rybicki 1987) shows that one can recover information about the density only outside a “cone of ignorance” of opening angle  $90^\circ - i$ . The deprojection of photometry for galaxies with  $i$  significantly less than  $90^\circ$  can thus be significantly in error because of undetermined konus densities (Gerhard & Binney 1996; Kochanek & Rybicki 1996).

Fortunately, NGC 4697 is seen almost edge-on and hence does not suffer from this ill-condition. Dejonghe et al. (1996) observed a nuclear dust lane with a ring-like appearance, elongated along the major axis of NGC 4697. Assuming that the ring is settled in the equatorial plane, they estimated an inclination angle  $i = 78^\circ \pm 5^\circ$ . Applying a disk-bulge decomposition to the isophote shapes of the galaxy, and assuming a thin disk, Scorza & Bender (1995) derived an inclination  $i = 67^\circ$ . This was updated by Scorza et al.

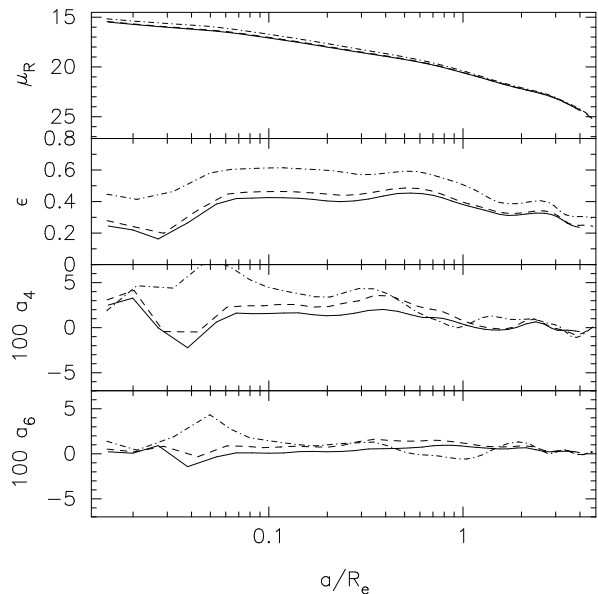


**Figure 2.** Isophote parameter profiles for the NGC 4697 photometry compared with those of the deprojected luminosity models shown in Figure 1 but now as seen in edge-on projection. NGC 4697 is coded as the solid line, whereas the  $i = 80^\circ$  and  $i = 67^\circ$  luminosity models are presented by the dashed and the dash-dotted lines, respectively.

(1998) to  $i = 70^\circ$ . Scorza & Bender (1995) also estimated the velocity dispersion  $\sigma_d$  of the disk component from the major axis line-of-sight velocity distributions. From their plots we estimate  $\sigma_d \simeq 95 \text{ km s}^{-1}$  at the half-mass radius of the disk,  $r_D \simeq 13''$ . Assuming that the vertical dispersion in the disk is comparable, we can estimate the intrinsic flattening of the disk  $\propto \sigma_d^2/v_c^2 \simeq 0.2$ , using the measured rotation velocity. A disk with intrinsic thickness  $h/R \simeq 0.2$  would give the same isophote distortions for inclination  $i \simeq 80^\circ$  as a thin disk with  $i = 67 - 70^\circ$ , in agreement with the value found by Dejonghe et al. (1996).

We have deprojected NGC 4697 for inclinations  $i = 90^\circ$ ,  $i = 80^\circ$  and  $i = 67^\circ$ , using the method and program of Magorrian (1999). This algorithm uses a maximum penalized likelihood method with a simulated annealing scheme to recover a smooth three-dimensional luminosity density distribution which, when projected onto the sky-plane, has minimal deviations from the observed SB. The three-dimensional luminosity density so obtained extends beyond the radial range of the data, where the penalized likelihood scheme favours an outer power-law density profile. Figure 1 compares the observed photometry with the three deprojected luminosity models reprojected on the sky. In the range from  $0.2R_e$  to  $2R_e$  the  $i = 67^\circ$  deprojection yields a significantly less good fit to the observed  $a_4$  and  $a_6$ . Figure 2 compares the radial run of the isophotal shape parameters for the  $i = 80^\circ$  and  $i = 67^\circ$  luminosity models projected edge-on, with the observed photometry of NGC 4697. The  $i = 80^\circ$  deprojection produces again somewhat better results. It is also more physical because it allows for a finite thickness of the inner disk of NGC 4697, as discussed above. Hence we will adopt it for the dynamical study of NGC 4697 to follow.

### 2.3 Kinematic Data

#### 2.3.1 Stellar-absorption line data

Long slit absorption line kinematics within  $\sim R_e$  have been reported, amongst other works, by Binney et al. (1990) and Dejonghe et al. (1996). The Binney et al. (1990) kinematic data (BDI data) consist of line-of-sight velocity  $v$  and velocity dispersion  $\sigma$  profiles along the major axis, along slits  $10''$  and  $20''$  parallel to the major axis, along the minor axis, and along a slit  $22''$  parallel to the minor axis. They are derived using the Fourier Quotient (FQ) method (Illingworth & Schechter 1982). Dejonghe et al. (1996) have published further  $v$  and  $\sigma$  measurements (DDVZ data) at various position angles, also measured with the FQ method.

Along the major and minor axes we have derived additional line-of-sight velocity distribution (LOSVD) kinematics from the high S/N integrated absorption line spectra obtained by Méndez et al. (2005) with FORS2 at the VLT, a slit width of 1 arcsec and seeing  $1'' - 1.5''$ . We refer to this paper for a description of the data acquisition and reduction. The LOSVDs were measured using the Fourier Correlation Quotient (FCQ) method, as in Bender et al. (1994) and Mehlert et al. (2000), and the K3III star HD132345 as a template. From these LOSVDs, profiles of  $v$ ,  $\sigma$ ,  $h_3$  and  $h_4$ , the Gauss-Hermite coefficients (Gerhard 1993; van der Marel & Franx 1993), were obtained; these are shown in Figure 3. Tables A1 and A2 give the data in tabular form. The statistical errors derived from Monte Carlo simulations are minute and much smaller than the rms scatter observed between the two sides of the galaxy. These differences are particularly obvious along the major axis in the radial range 10-20 arcsec. As noted in Méndez et al. (2005), in this region we detect patchy [OIII] emission that is affecting to some extent the kinematics. Judging from the asymmetries in the kinematics on both sides of the galaxy, we estimate the residual systematic errors affecting the data, which amount to  $\approx 3$  km/s in  $V$ ,  $\approx 3.5$  km/s in  $\sigma$ ,  $\approx 0.02$  in  $h_3$  and  $h_4$ .

In the following we discuss the comparison between the kinematic data derived here and the kinematics published in the literature. Note that part of the differences seen below arise from the different observational setups (along the major axis different slit widths probe different relative amounts of the central disk structure present in the galaxy and related [OIII] emission regions) and methods used. In particular, the FQ method fits Gaussian profiles to the LOSVDs, ignoring the higher order Gauss-Hermite terms. In general the systematic effect on the measured mean velocity and velocity dispersion profiles is small (van der Marel et al. 1994). When applied to our major axis data set, FQ gives systematically slightly smaller mean velocities and larger velocity dispersions.

In the inner 10 arcsec along the major axis we confirm the clear kinematic signature of the central disk discussed by Scorza & Bender (1995, SB) and agree well with their mean velocities and velocity dispersions derived also with the FCQ method and 1.8 arcsec slit width (see Figure 4, left, cyan points). Along the same axis we find good agreement with Fried & Illingworth (1994) (FI, yellow, derived using the FQ method and 1.1 arcsec slit width). Overall, the BDI data (Figure 4, red points, 2.6 arcsec slit width), agree well with our data, although at  $15''$  along the ma-

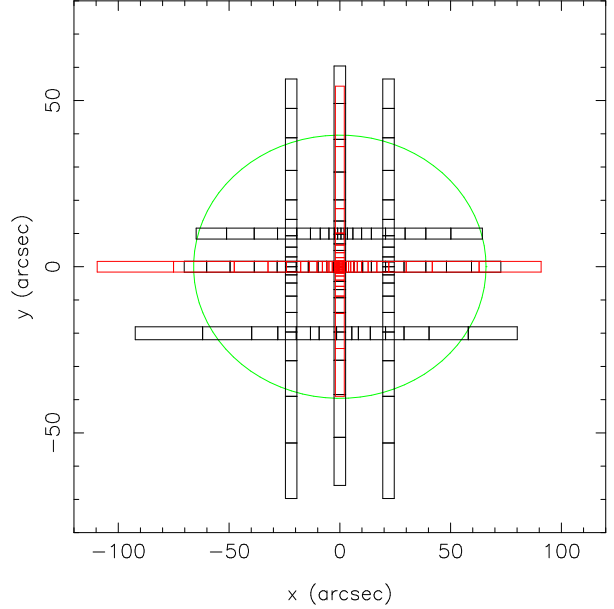


**Figure 5.** Schematic view of the slit setup used to construct the particle models. BDI slits are shown in black and our slits are shown in red. The ellipse has a semi-major axis of length  $R_e$  and axis ratio  $q = 0.6$ .

ior axis, the two data sets differ systematically. The  $\sigma$  profiles of DDVZ (blue points, 0.7 arcsec slit width) differ significantly in the sense that at small semi-major axis distances the DDVZ  $\sigma$  is increasing with radius but our  $\sigma$  is decreasing. Finally, the right panel of Figure 4 compares our data along the minor axis with the data sets of BDI (red points) and Koprolin et al. (2000) (KZ, green points, 2 arcsec slit width), who use the Fourier Fitting method of van der Marel & Franx (1993). Both agree within their respective (larger) errorbars.

Based on the radial extent and quality of the different datasets, and taking into account the discussion above, we have decided to use in the subsequent modeling only our data combined with BDI. For our kinematic data, the errors in  $v$  and  $\sigma$  are  $\lesssim 0.5 \text{ km s}^{-1}$ , which is small compared to the scatter in the data. This suggests, as already discussed above, that systematic errors dominate. For the modelling we have therefore replaced these errors with the smallest errors in  $v$  and  $\sigma$  of the BDI data along the major and minor axis, respectively ( $5 - 7 \text{ km s}^{-1}$ ). Similar arguments hold for  $h_3$  and  $h_4$  and we set their errors to 0.01. In addition, the  $h_3$  coefficients along the minor axis scatter significantly around zero while the minor axis velocities are consistent with zero; thus we replace these  $h_3$  values by  $h_3 = 0.0$ .

Figure 5 gives a schematic view of the arrangement of the kinematic slits used in the modelling process.

#### 2.3.2 Planetary nebula velocities

Planetary nebulae (PNe) are dying stars that emit most of their light in a few narrow lines of which the [OIII] $\lambda 5007$  is the most prominent one. The PN population in elliptical galaxies is expected to arise from the underlying galactic population of old stars and hence the PNe can be used as

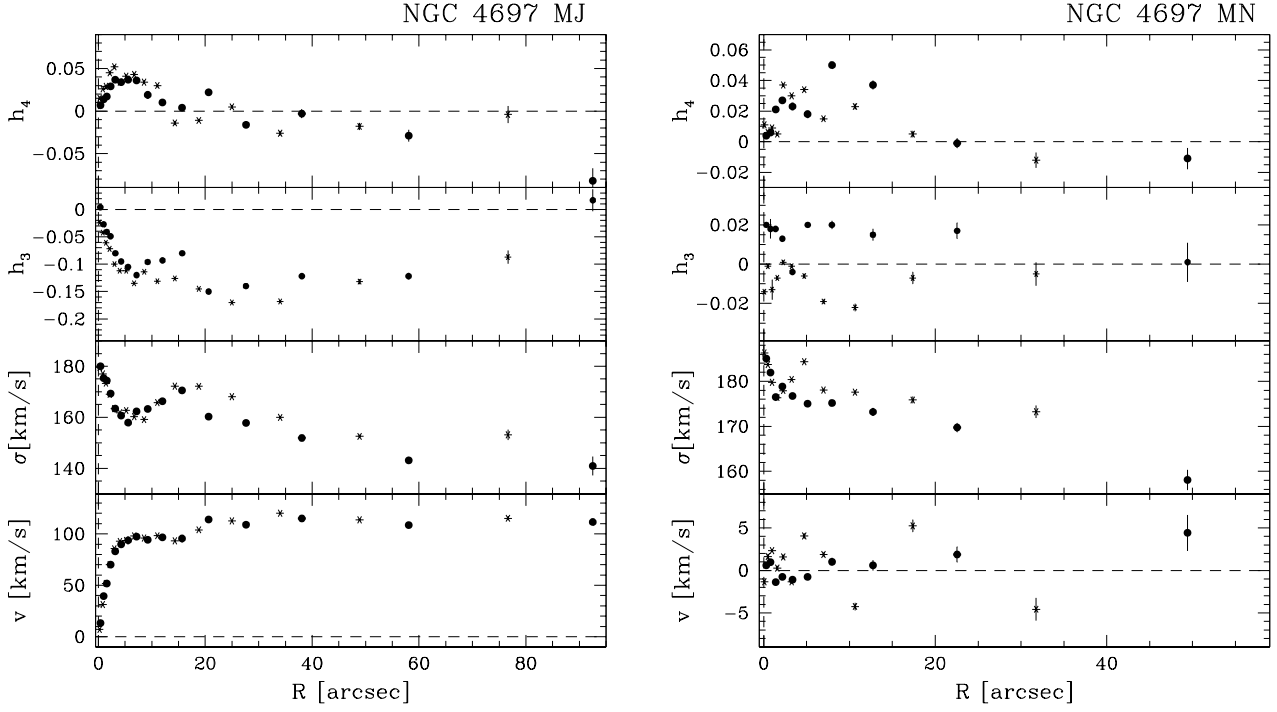


**Figure 3.** The kinematics along the major (left panel) and minor (right panel) axis of NGC 4697. The filled and starred symbols refer to the data folded along the axes.

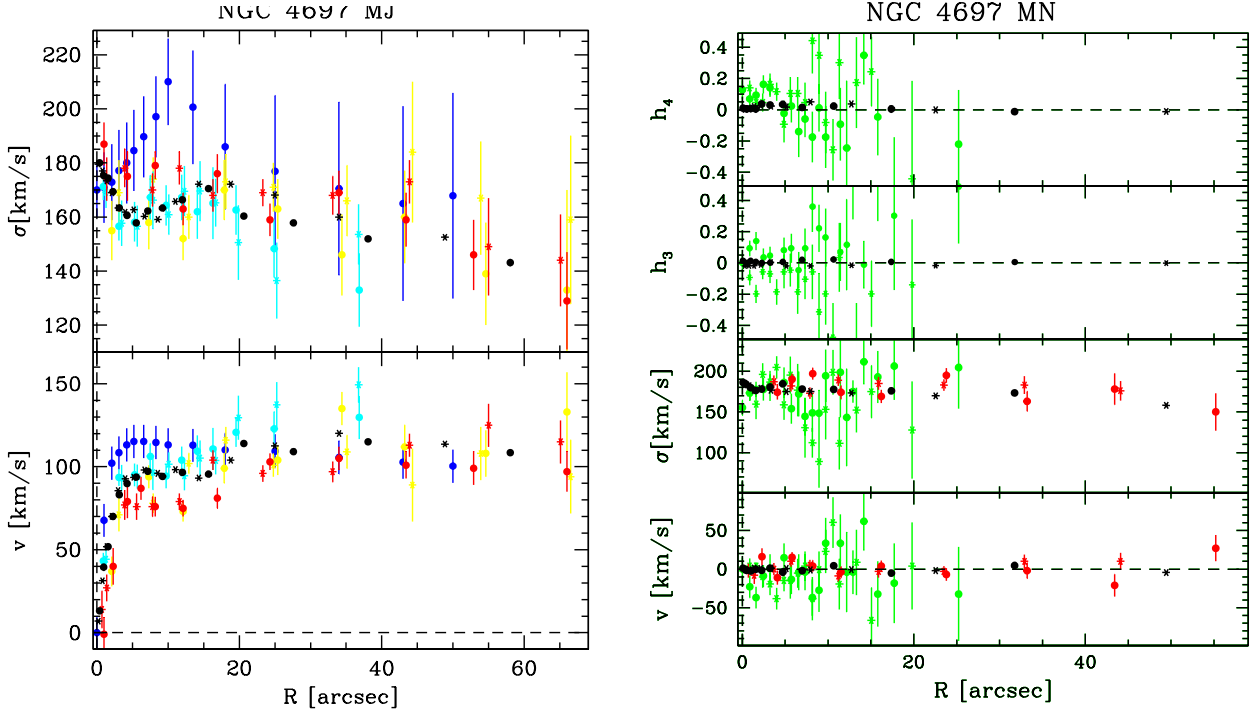


**Figure 4.** Comparison between the different absorption line kinematics along the major (left panel) and the minor (right panel) axis. Black: our data; red: BDI; blue: DDVZ; cyan: SB; green: KZ; yellow: FI.

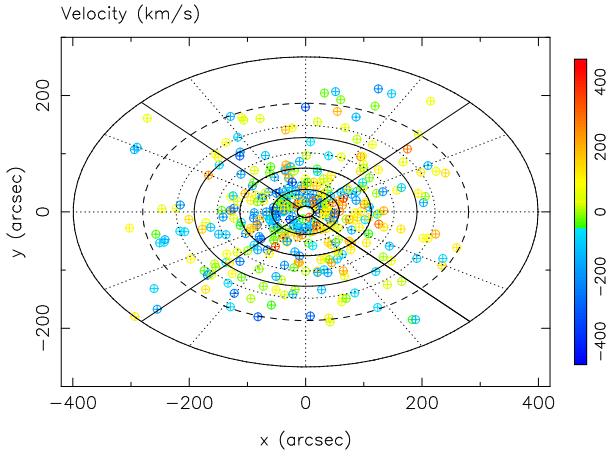


**Figure 6.** The positions and velocities of the cleaned PN sample of 381 PNe. The lines indicate the different grids used for binning the PNe. Details are given in the text.

kinematic tracers for the stellar distribution. Méndez et al. (2001) detected 535 PNe in NGC 4697 and were able to measure radial velocities for 531 of these with a typical error of  $40 \text{ km s}^{-1}$ .

Sambhus et al. (2006) analyzed the correlations between the magnitudes, velocities and positions of these 531 PNe and found kinematic evidence for more than one PN sub-population in NGC 4697. In addition to the main PN population, they found evidence for a population of preferably bright PNe which appeared to be not in dynamical equilibrium in the galactic potential. To remove these possible kinematic contaminants, and to also ensure completeness for  $R > R_e$  (Méndez et al. 2001), we discard all PNe with magnitudes outside the range  $26.2 < m(5007) \leq 27.6$ . The positions and velocities of the remaining 381 PNe are shown in Figure 6. In the following, we use a doubled sample of 762 PNe for our analysis, obtained by applying a point-symmetry reflection. Every PN with observed position coordinates  $(x, y)$  on the sky and line-of-sight velocity  $v_{PN}$  is reflected with respect to the center of the galaxy to generate a new PN with coordinates  $(-x, -y, -v_{PN})$ . Such point-symmetric velocity fields are expected for axisymmetric and non-rotating triaxial potentials. Moreover, this reflection will help to further reduce any PN sub-population biases which might still be present.

We compute  $v$  and  $\sigma$  on two slightly different spatial grids, subtracting  $40 \text{ km s}^{-1}$  in quadrature from all PN velocity dispersions to account for the measurement uncertainties (Méndez et al. 2001). We use the spatial bins defined by the solid lines displayed in Figure 6 to obtain data set PND1, which is shown together with the models in Section 5. The second data set, PND2, is computed using the same grid but replacing the outermost ellipse by the dashed ellipse with semi-major axis  $a = 280''$ . This second grid is used to make sure that the dynamical models we generate are not affected by the way we define the outermost bins.

### 3 NMAGIC MODELS

In this section we give a brief introduction to NMAGIC and present a few extensions to the method described in de Lorenzi et al. (2007). Syer & Tremaine (1996) invented a particle-based method for constructing models of stellar systems. This “made-to-measure” (M2M) method works by adjusting individual particle weights as the model evolves, until the N-particle system reproduces a set of target constraints. de Lorenzi et al. (2007) improved the algorithm to account for observational errors and to assess the quality of a model for a set of target data directly, using the standard  $\chi^2$  statistics in the function to be maximized upon convergence of the weights ( $\chi^2\text{M2M}$ ). NMAGIC is a parallel implementation of the improved  $\chi^2\text{M2M}$  algorithm.

#### 3.1 Luminous and dark matter distribution

##### 3.1.1 Luminous mass

We assume that the luminous mass distribution of NGC 4697 follows the deprojected luminosity density. The mass density of the luminous matter is then given by  $\rho_* = \Upsilon j$ , with mass-to-light ratio  $\Upsilon$  and luminosity density  $j$  represented by the discrete ensemble of particles with positions  $\mathbf{x}_i$  and luminosities  $L_i$ .

##### 3.1.2 Dark halo potential

The prevailing cosmological paradigm predicts that galaxies have massive, extended dark matter halos. Numerical cold dark matter (CDM) simulations reveal universal halo density profiles with steep central density cusps (*e.g.* Navarro et al. 1996; Moore et al. 1999). On the other hand, observations of many dwarf and low-surface brightness galaxies find shallower inner density cores (*e.g.* de Blok et al. 2003; McGaugh et al. 2007). Here our aim is not to determine the detailed shape of the dark matter halo in NGC 4697, but rather to first see whether the PN velocities allow or require any dark matter at all in this galaxy. To answer this question we will investigate a one-dimensional sequence of potentials whose circular velocity curves vary at large radii between the near-Keplerian decline expected when the mass in stars dominates, and the nearly flat shapes generated by massive dark halos. Thus for our dynamical studies of NGC 4697, we represent the dark matter halo by the logarithmic potential (Binney & Tremaine 1987)

$$\phi_D(R', z') = \frac{v_0^2}{2} \ln(r_0^2 + R'^2 + \frac{z'^2}{q_\phi^2}), \quad (1)$$

which is generated by the density distribution

$$\rho_D(R', z') = \frac{v_0^2}{4\pi G q_\phi^2} \frac{(2q_\phi^2 + 1)r_0^2 + R'^2 + 2(1 - \frac{1}{2}q_\phi^{-2})z'^2}{(r_0^2 + R'^2 + q_\phi^{-2}z'^2)^2}, \quad (2)$$

where  $v_0$  and  $r_0$  are constants,  $q_\phi$  is the flattening of the potential, and  $R'$  and  $z'$  are cylindrical coordinates with respect to the halo’s equatorial plane. When  $q_\phi < 1/\sqrt{2}$  the density becomes negative along the  $z'$  axis. The density given in equation 2 has a shallow inner density profile, but since we are mainly interested in the circular velocity curve in the outer halo of NGC 4697, this is inconsequential: it is always possible to reduce the stellar mass-to-light ratio

in exchange for an additional centrally concentrated dark matter cusp.

### 3.1.3 The total gravitational potential

The total gravitational potential is generated by the combined luminous mass and dark matter distributions and is given by

$$\phi = \phi_\star + \phi_D, \quad (3)$$

where  $\phi_\star$  is generated by the  $N$ -particle system assuming a constant mass-to-light ratio for each stellar particle. We estimate  $\phi_\star$  via a spherical harmonic decomposition (Sellwood 2003; de Lorenzi et al. 2007). The stellar potential is allowed to change during a NMAGIC modelling run, but the dark matter potential is constant in time and is given by equation (1). The particles are integrated in the global potential using a drift-kick-drift form of the leapfrog scheme with a fixed time step.

## 3.2 Model observables

Typical model observables are surface or volume densities and line-of-sight kinematics. An observable  $y_j$  of a particle model is computed via

$$y_j(t) = \sum_{i=1}^N w_i K_j[\mathbf{z}_i(t)], \quad (4)$$

where  $w_i$  are the particle weights,  $\mathbf{z}_i$  are the phase-space coordinates of the particles,  $i = 1, \dots, N$ , and  $K_j[\mathbf{z}_i(t)]$  is a kernel corresponding to  $y_j$ . We use units such that the luminosity  $L_i$  of a stellar particle can be written as  $L_i = L w_i$ , where  $L$  is the total luminosity of the model galaxy. We use temporally smoothed observables to increase the effective number of particles in the system, *cf.* Syer & Tremaine (1996); de Lorenzi et al. (2007).

### 3.2.1 Luminosity constraints

For modeling the luminosity distribution of NGC 4697 one can use as observables the surface density or space density on various grids, or some functional representations of these densities. We have chosen to model a spherical harmonics expansion of the deprojected luminosity density. We determine the expansion coefficients  $A_{lm}$  for the target galaxy on a 1-D radial mesh of radii  $r_k$ . The spherical harmonic coefficients for the particle model are computed via

$$a_{lm,k} = L \sum_i \gamma_{ki}^{CIC} Y_l^m(\theta_i, \varphi_i) w_i, \quad (5)$$

where  $L$  is the total luminosity of the model galaxy,  $w_i$  the particle weights,  $Y_l^m$  the spherical harmonic functions and  $\gamma_{ki}^{CIC}$  is a selection function, which maps the particles onto the radial mesh using a cloud-in-cell scheme (see de Lorenzi et al. 2007).

### 3.2.2 Kinematic constraints

Since in the  $\chi^2$ M2M algorithm the kernel in equation (4) cannot depend on the particle weights themselves, this puts

some constraints on which observables can be used. For kinematics, suitable observables are the luminosity-weighted Gauss-Hermite coefficients or the luminosity-weighted velocity moments. We implement them as follows.

*Spectroscopic data* The shape of the line-of-sight velocity distribution (LOSVD) can be expressed as a truncated Gauss-Hermite series and is then characterized by  $V$ ,  $\sigma$  and  $h_n$  ( $n > 2$ ), where  $V$  and  $\sigma$  are free parameters. If  $V$  and  $\sigma$  are equal to the parameters of the best fitting Gaussian to the LOSVD, then  $h_1 = h_2 = 0$  (van der Marel & Franx 1993; Rix et al. 1997). The luminosity-weighted Gauss-Hermite coefficients are computed as

$$b_{n,p} \equiv l_p h_{n,p} = 2\sqrt{\pi}L \sum_i \delta_{pi} u_n(\nu_{pi}) w_i, \quad (6)$$

with

$$\nu_{pi} = (v_{z,i} - V_p) / \sigma_p. \quad (7)$$

Here  $v_{z,i}$  denotes the line-of-sight velocity of particle  $i$ ,  $l_p$  is the luminosity in cell  $C_p$ ,  $V_p$  and  $\sigma_p$  are the best-fitting Gaussian parameters of the target LOSVD in cell  $C_p$ , and the dimensionless Gauss-Hermite functions are (Gerhard 1993)

$$u_n(\nu) = (2^{n+1} \pi n!)^{-1/2} H_n(\nu) \exp(-\nu^2/2). \quad (8)$$

$H_n$  are the standard Hermite polynomials and  $\delta_{pi}$  is a selection function which is one if particle  $i$  is in cell  $C_p$  and zero otherwise. The errors in  $h_1$  and  $h_2$  can be computed from those of  $V$  and  $\sigma$  via

$$\Delta h_1 = -\frac{1}{\sqrt{2}} \frac{\Delta V}{\sigma} \quad (9)$$

and

$$\Delta h_2 = -\frac{1}{\sqrt{2}} \frac{\Delta \sigma}{\sigma}, \quad (10)$$

valid to first order (van der Marel & Franx 1993; Rix et al. 1997). Since we use the observed  $V_p$  and  $\sigma_p$  from a Gauss-Hermite fit to the LOSVD as expansion parameters for the model line profiles, the final fitted  $h_1$  and  $h_2$  of a model will be small, and so we can also use relations (9) and (10) to compute the model  $V$  and  $\sigma$  from  $V_p$  and  $\sigma_p$ .

*Spatially binned PNe data* We have computed mean PN velocities and velocity dispersions for the ellipse sector bins shown in Figure 6. The ellipticity of the grid corresponds to the mean ellipticity of the photometry. As suitable observables we take the *luminosity-weighted* velocity moments in these bins, which are computed as

$$v_p^n = L \sum_i \delta_{pi} v_{z,i}^n w_i, \quad (11)$$

where  $v_{z,i}$  is the velocity along the line-of-sight of particle  $i$  and  $\delta_{pi}$  is a selection function, which is equal to one if particle  $i$  belongs to the bin segment under consideration and zero otherwise. In the following, we use only the moments  $v_p^1$  and  $v_p^2$ .

## 3.3 Seeing effects

To account for seeing effects we apply a Monte Carlo approach (*e.g.* Cappellari et al. 2006) instead of convolving



the observables with the PSF. As long as the particles move along their orbits no PSF effects need to be taken into account, only when the observables of the system are computed, the effects of seeing may matter.

When computing an observable including PSF effects, we replace the “original” particle at position  $(x_i, y_i)$  on the sky plane temporarily by a cloud of  $N_{pp}$  pseudo particles. The position of a pseudo particle is obtained by randomly perturbing  $(x_i, y_i)$  with probability given by the PSF. Note that neither extra storage is needed nor additional time to integrate the particles along their orbits. Usually, only a small number of pseudo particles are needed to model PSF effects, even one is often sufficient. This procedure is implemented in the kernel  $K_{ij}$  as defined in equation (4). The same kernel then enters the force-of-change equation, cf. de Lorenzi et al. (2007).

To test how well PSF effects are modeled using only a few pseudo particles we computed mock observations for a spherical isotropic galaxy of mass  $M = 10^{10} M_\odot$ , located at a distance 10 Mpc. The intrinsic density of the galaxy is given by a Hernquist (1990) profile with scale length  $a = 55.1''$ . We assumed a major axis slit of width  $2''$  and a Gaussian PSF with FWHM  $= 4''$ . We computed the LOSVD of the target galaxy along the major axis using higher order Jeans moments (Magorrian & Binney 1994), and compared it with the LOSVD of a particle realization of the mock galaxy, applying the above procedure. The particle realization of the Hernquist model was generated from an isotropic distribution function (e.g. Debattista & Sellwood 2000). As an example, Figure 7 shows the  $h_4$  profile along the major axis slit. The square symbols are the target data computed using higher order Jeans equations without seeing, the circles are computed the same way but including PSF effects. The lines are the temporally smoothed  $h_4$  profiles of the particle model using  $N_{pp} = 5$  to represent the PSF. One sees that the heavily seeing-affected central profile is well recovered by the model.

In the dynamical modeling of NGC 4697 we include seeing only for our new kinematic data. We represent the PSF by a single Gaussian with  $FWHM = 1.25''$ . For the BDI data we do not know the PSF but since the slit cells are relatively large, seeing is likely to be negligible.

### 3.4 The merit function

By fitting the particle model to the observables, the weights  $w_i$  are gradually changed such that the merit function

$$F = \mu S - \frac{1}{2} \chi^2 \quad (12)$$

is maximized, where  $S$  is a profit function and  $\chi^2$  measures the quality of the fit. The parameter  $\mu$  controls the relative contribution of the profit function to  $F$ ; incrementing  $\mu$  increases the influence of  $S$  in equation (12). The  $\chi^2$  statistics is computed as usual

$$\chi^2 = \sum_j \Delta_j^2, \quad (13)$$

where  $\Delta_j = (y_j - Y_j)/\sigma(Y_j)$ .  $y_j$  is a model observable (e.g.  $a_{lm,k}$  with  $\mathbf{j} = \{lm, k\}$ ),  $Y_j$  is the corresponding target and  $\sigma(Y_j)$  its error.

For the profit function  $S$ , we use the entropy

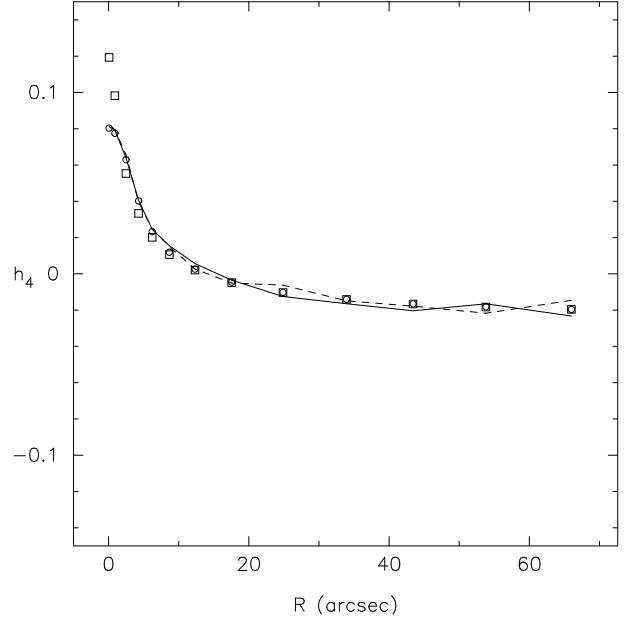


**Figure 7.** Seeing convolution test, comparing the radial run of  $h_4$  along a  $2''$  slit for a spherical target model and its particle representation. The squares (circles) were computed for the target from higher order Jeans equations without (with) seeing. The lines correspond to the particle model including seeing, for which the PSF was represented using  $N_{pp} = 5$ . The full and dashed lines refer to the major axis slit data at positive resp. negative radii with respect to the origin. The heavily seeing-affected central profile is well recovered by the model.

$$S = - \sum_i w_i \ln(w_i/\hat{w}_i) \quad (14)$$

where  $\{\hat{w}_i\}$  are a predetermined set of weights, the so-called priors (here equal for all particles). The entropy term pushes the particle weights to remain close to their priors (more specifically, close to  $\hat{w}_i/e$ ). This implies that models with large  $\mu$  will have smoother distribution functions than those with small  $\mu$ . The best choice for  $\mu$  depends on the observational data to be modeled, e.g. their spatial coverage, on the phase-space structure of the galaxy under consideration, but also on the initial conditions. For the dataset at hand, the best value of  $\mu$  will be determined in Section 4.1

### 3.5 Discrete PNe velocities

The likelihood of a model fit to photometric as well absorption line kinematic data is measured by the standard  $\chi^2$  statistics given in equation (13). To treat discrete PN velocity measurements the same way, we must bin them to estimate the underlying mean  $v$  and  $\sigma$  fields. This gives the corresponding model observables as discussed in section 3.2.2.

As an alternative, one can measure the likelihood of a sample of discrete velocities  $v_j$  and positions  $\mathbf{R}_j = (x_j, y_j)$  on the sky via

$$\mathcal{L} = \sum_j \ln \mathcal{L}_j \quad (15)$$



using the likelihood function for a single PN (Romanowsky & Kochanek 2001)

$$\mathcal{L}_j(v_j, \mathbf{R}_j) = \frac{1}{\sqrt{2\pi}} \int \frac{dL}{dv_z}(v_z, \mathbf{R}_j) e^{-(v_j - v_z)^2 / 2\sigma_j^2} dv_z, \quad (16)$$

where  $\sigma_j$  is the error in velocity and  $dL/dv_z$  is the LOSVD assuming as before that the line-of-sight is along the z-axis.

We can then add equation (15) to the function  $F$  given in equation (12) and maximize

$$F^+ = F + \mathcal{L} \quad (17)$$

with respect to the particle weights  $w_i$ . Hence, we obtain an additional contribution to the force-of-change as given in de Lorenzi et al. (2007). We will now derive this extra term. Let us consider the selection function

$$\delta_{ji} = \begin{cases} 1 & \text{if } (x_i, y_i) \in \mathcal{C}_j \\ 0 & \text{otherwise.} \end{cases}$$

which assigns particle weights to a spatial cell  $\mathcal{C}_j$ , which contains the  $j$ -th PNe. We can then write  $dL/dv_z$  at position  $j$  as

$$\left(\frac{dL}{dv_z}\right)_j = \frac{1}{l_j} \sum_i \delta_{ji} w_i \delta(v_z - v_{z,i}) \quad (18)$$

with

$$l_j = \sum_i \delta_{ji} w_i, \quad (19)$$

and  $\delta(x)$  being the standard delta function. Hence, equation (16) can be expressed in terms of the particles via

$$\mathcal{L}_j = \frac{\hat{\mathcal{L}}_j}{l_j} \quad (20)$$

with

$$\hat{\mathcal{L}}_j = \frac{1}{\sqrt{2\pi}} \sum_i \delta_{ji} w_i e^{-(v_j - v_{z,i})^2 / 2\sigma_j^2}. \quad (21)$$

Finally, we find for the additional term in the FOC

$$\frac{dw_i}{dt} = \varepsilon w_i \sum_j \delta_{ji} \left( \frac{1}{\sqrt{2\pi}} \frac{e^{-(v_j - v_{z,i})^2 / 2\sigma_j^2}}{\hat{\mathcal{L}}_j} - \frac{1}{l_j} \right), \quad (22)$$

where the sum runs over all individual PNe. For small errors, the  $dw_i/dt$  from the likelihood term is positive for particles with  $v_j = v_{z,i}$ , but reduces the weights of the other particles and hence drives the LOSVD to peak at  $v_j$ . In the implementation, we replace  $l_j$  and  $\hat{\mathcal{L}}_j$  with the corresponding temporally smoothed quantities.

When we use this method to account for the PN velocities in NGC 4697, we adopt the grid defined in Figure 6 by the dotted lines, including the innermost and outermost full ellipses. In this way, we assign each of the 762 PNe to a cell  $\mathcal{C}_j$ . It follows, that more than one PNe share the same spatial bin, but this is not a problem.

### 3.6 Efficient mass-to-light estimate

It is common practice to evolve N-particle systems in internal units (IU), in which the gravitational constant and the units of length and mass are set to unity, and to scale the system to physical units (PU) a posteriori to compare

with galaxy observations. Similarly, the velocities of a system with mass-to-light ratio  $\Upsilon$  of unity may be scaled to any  $\Upsilon$  via  $v_{\text{PU}} = \gamma v_{\text{IU}}$  where  $\gamma \propto \sqrt{\Upsilon}$  and  $v_{\text{PU}}$  and  $v_{\text{IU}}$  are the velocities in physical and internal units, respectively. It follows that the kinematic observables of the model and hence also  $\chi^2$  can be regarded as functions of  $\Upsilon$ . Equation (13) then reads

$$\chi^2 = \sum_j \Delta_j(\Upsilon)^2. \quad (23)$$

In the following we will only consider the luminosity-weighted Gauss-Hermite moments as given in equation (6) and neglect the PNe kinematic constraints. Taking the partial derivative with respect to  $\Upsilon$  of equation (23) leads to

$$\frac{1}{2} \frac{\partial \chi^2}{\partial \Upsilon} = \sum_j \frac{\Delta_j(\Upsilon)}{\sigma(B_{n,p})} \frac{\partial b_{n,p}}{\partial \Upsilon}, \quad \mathbf{j} = \{n, p\} \quad (24)$$

where  $B_{n,p}$  is the target observable and  $\sigma(B_{n,p})$  its error. We define a force-of-change (FOC) for the mass-to-light ratio  $\Upsilon$

$$\frac{d\Upsilon}{dt} = -\eta \Upsilon \frac{\partial \chi^2}{\partial \Upsilon} \quad (25)$$

which equals

$$\frac{d\Upsilon}{dt} = -\eta \Upsilon \sum_j 2\Delta_j(\Upsilon) \frac{\partial \Delta_j(\Upsilon)}{\partial \Upsilon} \quad (26)$$

with

$$\frac{\partial \Delta_j(\Upsilon)}{\partial \Upsilon} = \frac{\sqrt{\pi} L}{\Upsilon \sigma_p \sigma(B_{n,p})} \sum_i \delta_{pi} w_i \frac{\partial u_n(x)}{\partial x} \Big|_{x=\nu_{pi}} v_{z,i}, \quad (27)$$

where we used  $\partial v_{z,i} / \partial \Upsilon = v_{z,i} / 2\Upsilon$  for  $v_{z,i}$  given in physical units, and  $\mathbf{j} = \{n, p\}$ . The line-of-sight is along the z axis. In practice, we use the temporally smoothed quantities to compute the FOC for the mass-to-light ratio.

In principle, the proposed scheme can be understood as a gradient search along the  $\chi^2(\Upsilon)$  curve when simultaneously the particle model is fitted to the observational constraints. Hence the same NMAGIC run allows us to estimate  $\Upsilon$  as well. We test the scheme and illustrate its accuracy in Section 4.

### 3.7 Initial conditions

As initial conditions for NMAGIC, we generate a particle realization of a spherical  $\gamma$ -model (Dehnen 1993; Carollo et al. 1995) made from a distribution function (DF) using the method of Debattista & Sellwood (2000). The model consists of  $N = 5 \times 10^5$  particles and has  $\gamma = 1.5$ , scale length  $a = 1$  and  $r_{\text{max}} = 40$ . When scaled to NGC 4697 one unit of length corresponds to 2.3810 kpc, i.e., this model has  $R_e = 3.8$  kpc.

In some cases, we have found it useful to give the initial particle system some angular momentum about an axis of symmetry. For axisymmetric stellar systems, the density is determined through the even part in  $L_z$  of the DF (Lynden-Bell 1962). Thus the component of the angular momentum of a particle along the symmetry axis may be reversed without affecting the equilibrium of the system. Kalnajs (1977) showed, however, that a discontinuity at

$L_z = 0$  can affect the stability of the particle model. Therefore, if desired, we switch retrograde particles with a probability

$$p(L_z) = p_0 \frac{L_z^2}{L_z^2 + L_0^2}, \quad (28)$$

which ensures a smooth DF.

#### 4 TESTING THE MODELLING WITH ISOTROPIC ROTATOR TARGETS

In this section, we use axisymmetric, isotropic rotator models with known intrinsic properties to determine the optimal value of the entropy “smoothing” parameter  $\mu$  in equation (12), and to test our procedure for determining the optimal mass-to-light ratio simultaneously with modelling the data.

##### 4.1 Entropy parameter $\mu$

Our approach to determine suitable values for  $\mu$  is similar as in Gerhard et al. (1998); Thomas et al. (2005). We first generate a “mock” kinematic data set from an isotropic rotator model whose information content (number and density of points, errors) is similar as for the real data set to be modelled. To this data set we perform a sequence of particle model fits for various  $\mu$ , and determine the values of  $\mu$  for which (i) a good fit is obtained, and (ii) the known intrinsic velocity moments of the input “mock” system are well reproduced by the corresponding moments of the final particle model. Using an isotropic rotator model for this purpose here makes sense, because such a model is a fair representation of NGC 4697 (Binney et al. 1990). We have chosen to describe the luminosity density of the mock galaxy by one of the flattened  $\gamma$ -models of Dehnen & Gerhard (1994),

$$j(m) = \frac{(3 - \gamma)L}{4\pi q} \frac{a}{m^\gamma(m + a)^{4-\gamma}}. \quad (29)$$

Here  $L$  and  $a$  are the total luminosity and scale radius,  $m^2 = R'^2 + (z'/q)^2$ , and  $q$  is the flattening. The parameters are chosen such that the surface brightness closely resembles that of NGC 4697, i.e.,  $q = 0.7$ ,  $\gamma = 1.5$ ,  $L = 2 \times 10^{10} L_{\odot,R}$  and  $a = 2.5$  kpc, which corresponds to  $a \approx 49''$  at a distance of 10.5 Mpc. Figure 8 shows a comparison of the surface brightness of NGC 4697 with the mock galaxy projected under  $i = 80^\circ$ . The major and minor axis surface brightness profiles are well approximated by the  $\gamma$ -model, except for some differences at larger radii, so we will use this model for the calibration of  $\mu$ .

We determine mock kinematic profiles from internal velocity moments, obtained from higher-order Jeans equations (Magorrian & Binney 1994) in the self-consistent potential generated by the density of equation (29) for a mass-to-light ratio  $\Upsilon = 5$ . Before calculating the line-of-sight velocity profiles, the velocity moments are slit-averaged to account for the observational setup of the kinematic slits given in Section 2.3. We add Gaussian random variates to the isotropic rotator kinematics with  $1\sigma$  dispersion corresponding to the respective measurement error in NGC 4697 at that position. Figure 9 shows a comparison of our new kinematic data for NGC 4697 with the isotropic rotator mock data, along the galaxy’s major axis.

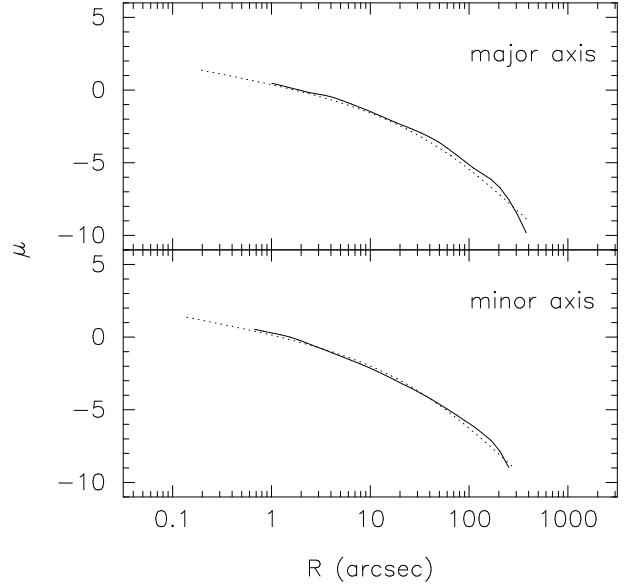


**Figure 8.** Comparison of the surface brightness of NGC 4697 (solid lines) with the  $\gamma$ -model described in the text and seen under  $i = 80^\circ$  inclination (dotted lines). Top: Surface brightness profile along the major axis. (b) Along the minor axis.

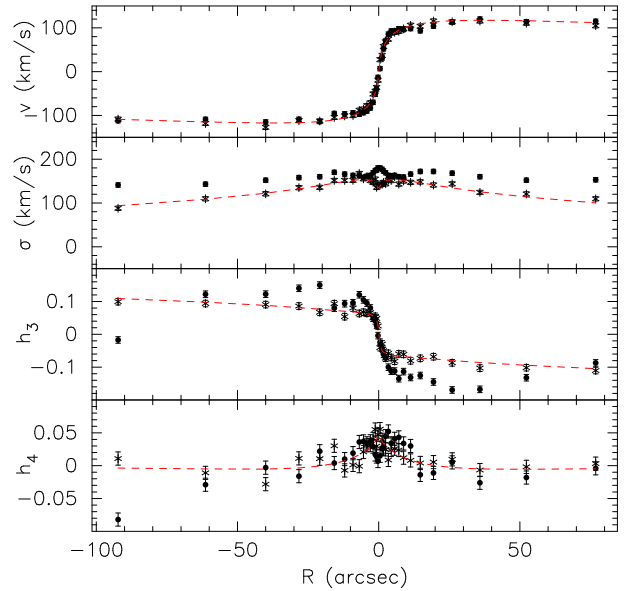


**Figure 9.** Comparison of  $v$ ,  $\sigma$ ,  $h_3$  and  $h_4$  of NGC 4697 and an isotropic rotator model with approximately the same projected surface brightness as the galaxy. The filled circles show our new kinematic data for NGC 4697 from Section 2.3, the star symbols show the isotropic rotator mock data, and the dashed red lines show the underlying smooth model kinematics, all along the major axis.

We do not construct mock PNe data for inclusion in the entropy tests, but we need to compute the photometric observables to construct a complete observational data set. We expand the luminosity distribution of equation (29) in a spherical harmonics series (*cf.* Section 3.2.1) on a radial grid with 40 shells at radii  $r_k$ . The radii are quasi-logarithmically spaced with  $r_{\min} = 1.0''$  and  $r_{\max} = 700''$ . We use the lumi-

osity on radial shells  $L_k = \sqrt{4\pi} A_{00,k}$  and the higher order coefficients  $A_{20,k}$ ,  $A_{22,k}$ ,  $\dots$ ,  $A_{66,k}$  and  $A_{80,k}$  to constrain the luminosity distribution of the particle model. The  $m \neq 0$  terms are set to zero to force the models to remain nearly axisymmetric, i.e., within the limits set by the  $A_{lm}$  errors. We assume Poisson errors for the  $L_k$ :  $\sigma(L_k) = \sqrt{L_k L/N}$  where  $N$  is the total number of particles used in the particle model and  $L$  is the total luminosity of the system. To estimate the errors in the higher order luminosity moments, we use Monte-Carlo experiments in which we generate particle realizations of a spherical approximation of the density field of the target system with  $5 \times 10^5$  particles, which is the same number as in the  $\chi^2$ M2M models for NGC 4697.

We then construct self-consistent particle models for the isotropic rotator target in a three step process, using the mock data as constraints. (i) Density fit: we start with the spherical initial conditions described in Section 3.7 and evolve them using NMAGIC to generate a self-consistent particle realization with the desired luminosity distribution ( $\gamma$ -particle model), fitting only the luminosity constraints. (ii) Kinematic fit: because the target galaxy has a fair amount of rotation, it is worth starting the kinematic fit from a rotating model. Hence, following Section 3.7, we switch a fraction of retrograde particles in the  $\gamma$ -particle model to prograde orbits, using  $p_0 = 0.3$  and  $L_0 \simeq L_{\text{circ}}(0.03R_e)$ . This rotating system we then use as a starting point to construct a series of self-consistent dynamical isotropic rotator models, by fitting the target photometry and kinematics for different values of  $\mu$ . For each model, we evolve the particle system for  $\sim 10^5$  NMAGIC correction steps while fitting the complete set of constraints. During this correction phase, the potential generated by the particles is updated after each correction step. (iii) Free evolution: to ensure that any correlations which might have been generated during the correction phase are phase-mixed away, we now keep the potential constant and evolve the system freely for another 5000 steps, without further correction steps. For reference, 5000 of these steps correspond to  $\approx 20$  circular rotation periods (“dynamical times”) at  $R_e$  in spherical approximation.

The results are presented in Figure 10. The lower panel shows the quality of the fit as a function of  $\mu$ , both in terms of normalized  $\chi^2$  values and in terms of the merit function  $F$  from equation (12). The upper panel shows the rms  $\Delta$  relative difference between the internal velocity moments of the isotropic rotator input model and those of the particle models reconstructed from the mock kinematics. For the particle models intrinsic velocity moments are computed by binning the particles in spherical polar coordinates, using a quasi-logarithmic grid with 20 radial shells bounded by  $r_{\text{min}} = 0.01''$  and  $r_{\text{max}} = 200''$ , 12 bins in azimuthal angle  $\phi$ , and 21 bins equally spaced in  $\sin \theta$ . The rms  $\Delta$  shown in Figure 10 is obtained by averaging over all grid points in the radial region constrained by the data ( $R \leq 1.5R_e$ ). The minimum in rms  $\Delta$  determines the value of  $\mu$  for which the model best recovers the internal moments of the input model. This occurs at  $\mu \simeq 10^3$ , and the value of rms  $\Delta$  at the minimum is  $\simeq 1.4\%$ . For larger (smaller)  $\mu$ , the rms  $\Delta$  is larger because of oversmoothing (excess fluctuations) in the model.

$\chi^2/N$  values are given in the lower panel of Fig. 10 for all (photometric and kinematic) data points, and for

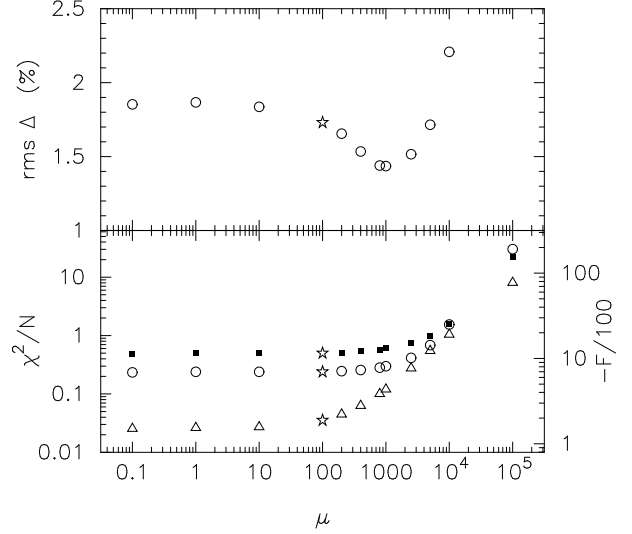


**Figure 10.** Entropy tests. Top: Deviation rms  $\Delta(\mu)$  of the particle models from the isotropic rotator internal velocity moments. The point for the rightmost value of  $\mu$  is at a large value of  $\Delta$  outside the diagram. Bottom:  $\chi^2$  deviation per data point of the particle model fit to the photometric and kinematic target observables (open circles) and to the kinematic observables alone (filled squares), as a function of entropy parameter  $\mu$ . The triangles show the same dependence for the merit function ( $-F$ ), cf. equation (12). The starred symbol indicates the value of  $\mu$  chosen for the subsequent modelling.

the kinematic data points alone. Generally the  $\chi^2/N$  for the photometric points is significantly better than for the kinematic points, because (i) the  $A_{lm}$  come from averages over many particles, thus have little noise, and we have not added Gaussian variances, and (ii) all particles contribute to the  $A_{lm}$  force-of-change at all timesteps, so the  $A_{lm}$  are weighted strongly during the evolution. The kinematic  $\chi^2$  per data point in the lower panel is of order 0.5 for a large range of  $\mu$  and then increases starting from  $\mu \gtrsim 300$  to 1 at  $\mu \simeq 5 \times 10^3$ , whereas  $-F$  already increases around  $\mu \gtrsim 100$ .

Some results for the isotropic rotator dynamical models obtained with  $\mu = 10^2$ ,  $\mu = 10^3$ ,  $\mu = 5 \times 10^3$  are presented in Figures 11 and 12. Figure 11 shows a comparison of the target kinematics with the kinematics of the self-consistent particle models along the major axis slit. Note the excellent fit of the central velocity gradient and velocity dispersion dip, for all  $\mu$  values. However, the models with higher  $\mu$  begin to fail matching the target data at the largest radii. This is because the number of data points decreases with radius, whereas the number of particles and hence entropy constraints is roughly proportional to luminosity  $L_k$ , i.e. changes much more slowly with radius. The result is that the constraints from the data become relatively weaker at larger radii. The entropy term tries to enforce a dynamical structure related to the initial particle model, in which all particles have equal weights. In the present case this works to cause a bias against both fast rotation and anisotropy. This first becomes apparent where the relative statistical power of the data is weakest, i.e., at large radii.

Because our goal in this paper is to determine the range of potentials in which we can find valid dynamical models for NGC 4697, we need to ensure that the answer to this ques-

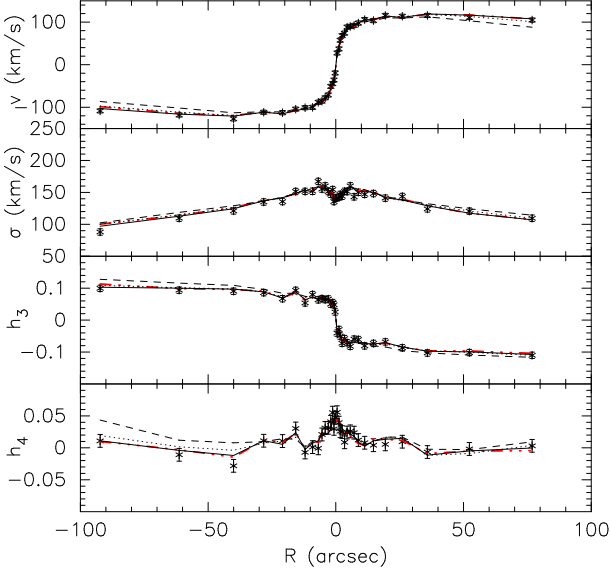


**Figure 11.** Particle model fits to the isotropic rotator mock kinematic data along the model’s major axis. The points with error bars show the target data and the lines represent the model kinematics. The model data points are averages over the same slit cells as the target data (see Fig. 5), and are connected by straight line segments. The model  $v$ ,  $\sigma$  are determined via eqs. (9) and (10) and  $h_3$ ,  $h_4$  are the fitted values based on the observed scale parameters  $V_p$  and  $\sigma_p$ . The full, dotted and dashed lines correspond to the models obtained with  $\mu = 10^2$ ,  $\mu = 10^3$ , and  $\mu = 5 \times 10^3$ , respectively. The red dashed line shows the  $\mu = 100$  model kinematics 20 dynamical times later, reflected with respect to the origin, and obtained from direct fitting of the model line profiles. This proves that this model is accurately axisymmetric and stationary; see text for details.

tion is not biased by overly strong entropy smoothing in the galaxy’s outer regions. Thus in the modelling in Section 5 we will conservatively choose  $\mu = 100$  for the smoothing parameter (indicated by the starred symbol in Fig. 10). Similar caution is common practice in determining black hole masses in galaxies (e.g., Gebhardt et al. 2003). The resulting dynamical models will then be somewhat less smooth than could be achieved, but this price is rather modest; between  $\mu = 10^2$  and its minimum value at  $\mu = 10^3$ , the rms  $\Delta$  in Fig. 10 decreases from  $\simeq 1.7\%$  to  $\simeq 1.4\%$ , i.e., by  $\simeq 15\%$ . Certainly it would not be appropriate to rule out potentials in which the solutions differ by this degree in smoothness.

Using  $\mu = 100$  in the modelling leads to a slight overfitting of the slit kinematic data, especially for the higher order kinematic moments which themselves take only values of order percents. It is worth pointing out that, contrary to first appearances from Fig. 11, this implies neither that these models are not axisymmetric, nor that they are out of equilibrium. The model kinematics shown in Fig. 11 are obtained after 20 dynamical times of free evolution in the axisymmetric potential, so are thoroughly phase-mixed. The model data points shown are averages over the same slit cells as the target data (see Fig. 5), and are connected by straight line segments. The plotted  $v$ ,  $\sigma$  are determined via eqs. (9) and (10) and  $h_3$ ,  $h_4$  are the fitted values based on the observed scale parameters  $V_p$  and  $\sigma_p$ . The red dashed line in Fig. 11 also corresponds to the  $\mu = 100$  model, but

has been determined as follows: (i) from the particle distribution after a total of 40 dynamical times of free evolution; (ii) from a mirror-symmetric set of slit cells, with respect to the major-axis slit shown in Fig. 5, (iii) using the  $(v, \sigma, h_3, h_4)$  parameters obtained by direct fits to the model line profiles, and (iv) finally reflecting the kinematics so obtained anti-symmetrically with respect to the origin. The excellent agreement between this curve and the original major axis kinematics of this model in Fig. 11 shows that (i) the  $\mu = 100$  model is a true equilibrium, (ii) it is accurately axisymmetric, and (iii) the left-right differences in the kinematics in Fig. 11 are due to slightly different slit cell averages over the model on both sides. That these averages can be slightly different is made possible by low-level (axi-symmetric) structure in the model consistent with the slight under-smoothing for this value of  $\mu$ . What happens is that the algorithm adds a few near-circular orbits in the relevant radial ranges. When added to the corresponding model LOSVDs and averaged over the asymmetric slit cells these orbits change the kinematic moments  $h_n$ ,  $n \geq 3$  at the  $\simeq 0.01$  level so as to improve the agreement with the observed major axis  $h_3$ ,  $h_4$ . In the other slits the models interpolate more smoothly between points when needed because fluctuations in the particle distribution to follow local kinematic features are less easily arranged; see the corresponding figure for NGC 4697 in Section 5.

A comparison of the internal velocity moments of the input model and the particle model in the equatorial plane is presented in Figure 12. The figure shows  $\sigma_R$ ,  $\sigma_\phi$  and  $\sigma_z$ , followed by  $v_\phi$ . The last panel displays the anisotropy parameter  $\beta_\theta = 1 - \sigma_\theta^2/\sigma_r^2$ , which is zero for the input isotropic rotator model. Within the radial extent of the target data, the internal moments of the input model are well reproduced; outside this region, where the model is poorly constrained by the input data, the particle model increasingly deviates from the target. Indeed, if we add PN velocity data in this test, the corresponding particle model agrees with the internal moments of the input model out to larger radii.

## 4.2 Mass-to-light ratio

We will now use such isotropic rotator models to explore how accurately we are able to recover the input mass-to-light ratio, given the spatial coverage of the data. Further, we will test our new procedure, described in Section 3.6, for estimating the mass-to-light ratio efficiently. As input models we take both the self-consistent isotropic rotator model described above and a model constructed in the same way but including a dark matter halo. The halo potential is of the form of equation (1), with  $r_0 = 190$  arcsec (9.7 kpc),  $v_0 = 220$  km s $^{-1}$  and  $q_\phi = 1.0$ . The mass-to-light ratio of the stars in both input models is fixed to  $\Upsilon = 5$ .

The results for a “classical” approach, in which we fit a dynamical particle model to the data for different values of  $\Upsilon$ , are presented in Figure 13, which shows the quality of the fit as function of  $\Upsilon$  for the self-consistent case. The input value of  $\Upsilon$  is recovered well. The results with the new procedure presented in Section 3.6 are summarized in Figure 14. The figure shows the evolution of the mass-to-light ratio as a function of time during NMAGIC model fits. Models for both the self-consistent input galaxy and for the target

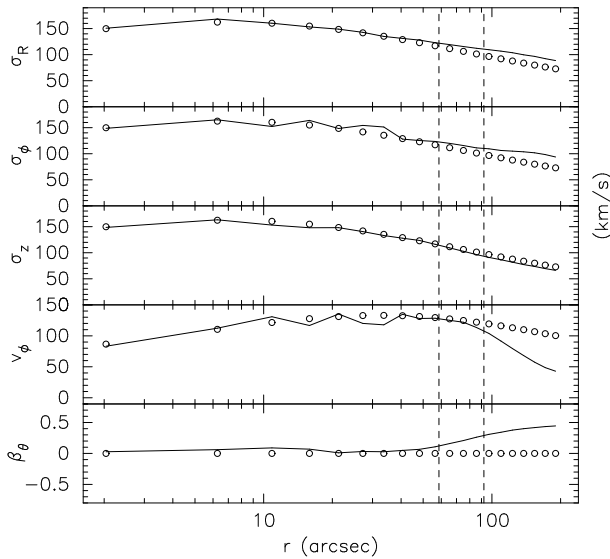


**Figure 12.** Comparison of the intrinsic velocity moments in the equatorial plane of the axisymmetric isotropic rotator particle model and target model. The points represent the target system and the lines correspond to the final particle model for  $\mu = 100$ , averaged over azimuth. The dashed vertical lines show the maximum radial extent of the minor axis (left line) and major axis target kinematic data (right line). At larger radii the particle model is poorly constrained by the input target data.

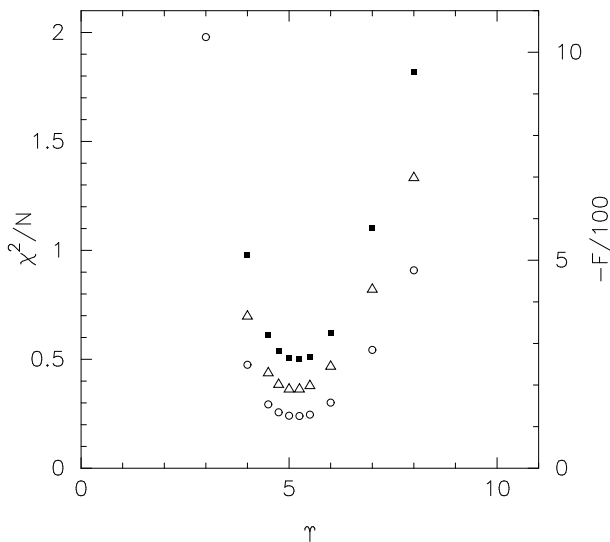


**Figure 13.** Quality of the particle model fit to the self-consistent isotropic rotator input model, as a function of assumed mass-to-light ratio  $\Upsilon$ .  $\chi^2$  values per data point are given for the particle model fit to the photometric and kinematic target observables (open circles) and to the kinematic observables alone (filled squares). The triangles correspond to the measured merit function  $F$ . The input mass-to-light ratio is  $\Upsilon = 5$ . All models are built using  $\mu = 100$ .

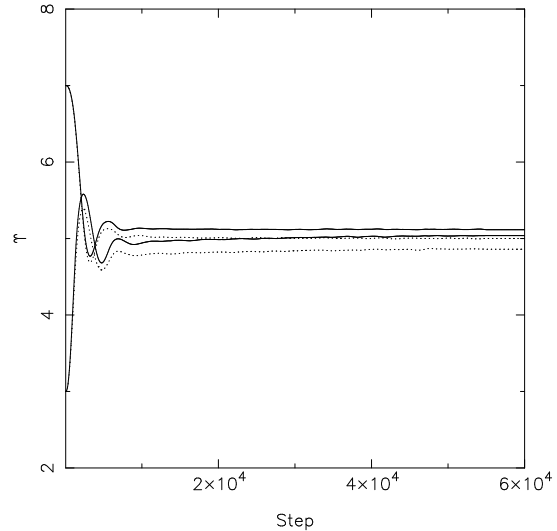


**Figure 14.** Direct mass-to-light ratio fits with NMAGIC. The plot shows the evolution of  $\Upsilon$  with time during NMAGIC runs with different initial  $\Upsilon$ , for the self-consistent isotropic rotator target (solid lines), and the isotropic rotator in a potential including a dark halo (dotted lines). The input mass-to-light ratio  $\Upsilon = 5$  in all cases. Time is given in terms of elapsed time steps where  $10^4$  steps correspond to  $\simeq 40$  circular rotation periods at  $1R_e$ .

model including a dark halo potential are shown, with both low and high initial choices of  $\Upsilon$ . The tests show that for the self-consistent case the input mass-to-light ratio is recovered very well. The uncertainties are slightly larger when a dark matter halo is included, but the maximum fractional error is less than three percent. We conclude that the new scheme works very well and that  $\Upsilon$  is recovered within a few percent (for the amount and quality of data used in the present work). The advantage of the new method is its efficiency, only one run is needed to estimate  $\Upsilon$  instead of order 10, but at the cost of not knowing the shape of  $\chi^2$  as a function of  $\Upsilon$  near the minimum, i.e., the confidence interval.

## 5 DYNAMICAL MODELS OF NGC 4697

After these tests we are now ready to use NMAGIC for constructing axially symmetric dynamical models of NGC 4697. We investigate self-consistent models as well as models including dark matter halos, and fit the photometry, slit kinematics and PNe data. Our aim in this paper is not to attempt to constrain detailed halo mass profiles, but only to ascertain whether a dark matter component is allowed, or required, by the kinematic data. Thus we investigate a simple sequence of potentials A to K which include the contribution from the stellar component and a halo potential as in equation (1), with parameters given in Table 1. The parameters are chosen to result in a sequence of circular speed curves ranging from falling according to the distribution of stars to nearly flat over the whole range of radii. This sequence is shown in Figure 15; all these circular velocity curves are computed in the galaxy's equatorial plane and include the stellar component with the respective best-fitting mass-to-light ratio as given in Table 1.

HALO	$r_0/R_e$	$v_0/\text{km s}^{-1}$	$q_\phi$	$\chi^2/N$	$\chi^2_{alm}/N_{alm}$	$\chi^2_{sl}/N_{sl}$	$\chi^2_{PN}/N_{PN}$	$-F$	$\Upsilon$
A	0	0	1.0	0.453	0.0323	0.900	0.968	370.2	5.78
B	5.76	80	1.0	0.415	0.0254	0.828	0.884	343.9	5.74
C	5.76	120	1.0	0.439	0.0343	0.877	0.784	358.6	5.71
D	4.32	160	1.0	0.404	0.0288	0.816	0.610	333.7	5.58
E	4.32	190	1.0	0.404	0.0244	0.826	0.520	332.8	5.49
F	4.32	210	1.0	0.386	0.0229	0.791	0.476	320.0	5.45
G	4.32	210	0.8	0.382	0.0203	0.785	0.439	315.4	5.46
H	2.88	210	0.8	0.376	0.0232	0.773	0.397	310.2	5.28
J	4.32	250	0.8	0.383	0.0242	0.786	0.377	313.7	5.34
K	2.88	250	0.8	0.377	0.0212	0.771	0.506	309.6	5.10

**Table 1.** Table of model parameters and fit results. Columns (1)-(4) give the model code and the parameters  $r_0$ ,  $v_0$  and  $q_\phi$  used in equation (1) for the respective dark halo potential in this model. The next four columns list the  $\chi^2$  values per data point, for all observables [column (5)], and for the density constraints, slit kinematic observables, and PN observables (data set PND1) separately [columns (6)-(8)]. Column (9) gives the numerical value of the merit function in equation 12, and column (10) the final (r-band) mass-to-light ratio. The respective number of constraints are  $N = 1316$ ,  $N_{alm} = 680$ ,  $N_{sl} = 604$ ,  $N_{PN} = 32$ .

HALO	$r_0/R_e$	$v_0/\text{km s}^{-1}$	$q_\phi$	$\chi^2/N$	$\chi^2_{alm}/N_{alm}$	$\chi^2_{sl}/N_{sl}$	$-\mathcal{L}$	$-F$	$\Upsilon$
A	0	0	1.0	0.415	0.0331	0.845	2042.9	2382.5	5.81
B	5.76	80	1.0	0.405	0.0282	0.830	2038.2	2371.5	5.76
C	5.76	120	1.0	0.419	0.0331	0.853	2033.7	2374.2	5.72
D	4.32	160	1.0	0.406	0.0314	0.828	2028.3	2357.9	5.60
E	4.32	190	1.0	0.391	0.0271	0.801	2026.3	2344.9	5.54
F	4.32	210	1.0	0.402	0.0304	0.820	2025.6	2350.1	5.49
G	4.32	210	0.8	0.396	0.0232	0.815	2024.8	2343.9	5.48
H	2.88	210	0.8	0.373	0.0245	0.766	2026.3	2329.2	5.31
J	4.32	250	0.8	0.374	0.0203	0.773	2025.6	2329.0	5.37
K	2.88	250	0.8	0.369	0.0198	0.763	2030.8	2329.9	5.14

**Table 2.** Table of model parameters and fit results, similar to Table 1, but with all models computed using the likelihood scheme for the PNe as discrete kinematic tracers. Columns (8) and (9) now give the likelihood of the PN data set  $\mathcal{L}$  and the merit function including  $\mathcal{L}$  [equation 17]. The other columns are equivalent to those in Table 1.

To construct the models, we proceed as in Section 4. First, we compute the photometric observables. We expand the deprojected luminosity distribution of NGC 4697 in a spherical harmonics series on a grid of 40 shells in radius, quasi-logarithmically spaced with  $r_{\min} = 1.0''$  and  $r_{\max} = 700''$ . As observables we use the luminosity on radial shells  $L_k$  and the higher order coefficients  $A_{20,k}$ ,  $A_{22,k}$ ,  $\dots$ ,  $A_{66,k}$  and  $A_{80,k}$ , at radii  $r_k$ . The  $m \neq 0$  terms are set to zero to force the models to remain nearly axisymmetric, i.e., within the limits set by the specified  $A_{lm}$  errors. Because the photometry is not seeing-deconvolved, for the innermost two points ( $R < 3''$ ) we only fit the  $A_{00}$  term. Errors for the luminosity terms  $A_{lm}$  are estimated by Monte Carlo simulations as in Section 4.1. As kinematic constraints we use the luminosity weighted Gauss-Hermite moments from the slit data, and the PNe kinematics, either represented by binned line-of-sight velocity and velocity dispersion points, or as discrete velocity measurements; see Sections 2.3.2 and 3.5.

Again we fit particle models in a three step process. (i) First, we start with the spherical particle model described in Section 3.7 and evolve it using NMAGIC to generate a self-consistent particle realization with the luminosity distribution given by the deprojection of the photometry. (ii) Because NGC 4697 shows significant rotation, we then switch retrograde particles similarly as in Section 4.1, us-

ing  $p_0 = 0.3$  and  $L_0 \simeq L_{\text{circ}}(0.03R_e)$ . The resulting rotating particle model (hereafter, model RIC) is used as a starting point to construct a series of dynamical models by fitting the photometry and kinematics in different halo potentials, as follows. For every dark matter halo from Table 1, we first relax RIC for 5000 time steps in the total gravitational potential, assuming a mass-to-light ratio of 5.74. For reference, 10000 time steps in the self-consistent potential correspond to  $\approx 40$  circular rotation periods at  $R_e$  in spherical approximation. After this relaxation phase, we evolve the particle system for  $\sim 10^5$  NMAGIC correction steps while fitting the complete set of constraints. During this correction phase, the potential generated by the particles is updated after each correction step but the dark matter potential (if present) is constant in time. (iii) Subsequently, we keep the global potential constant and evolve the system freely for another 5000 steps, without further correction steps. Models A, D, G and K were in addition evolved for a further 10000 steps with all potential terms active, to confirm that the modest radial anisotropy required in these models does not lead to dynamical instabilities.

To make sure that the results are not biased by the way we incorporate the PNe data, we have constructed three models in most halo potentials. Each time the PNe data are

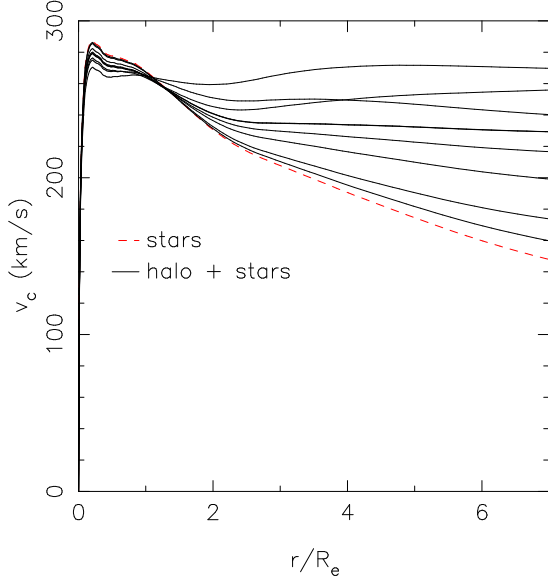


**Figure 15.** Circular velocity curves of the potentials used in the modelling, including the self-consistent model A (dashed line), and a sequence of dark matter halos (solid lines). The lines at  $r/R_e = 7$  run from model A (bottom) to K (top), with models F and G represented by the same curve; cf. Table 1.

represented differently, using the binnings PND1, PND2, or the likelihood method.

The quality of the fit for different halo models can be characterized by the quantity  $F$  defined in equation (12) or (17) and is given in Tables 1 and 2. In addition, the value of  $\chi^2$  per data point is also shown, globally and for each data set separately, as are the stellar mass-to-light ratios. For the same reasons as for the isotropic rotator test models, the density constraints are very accurately fit. The slit kinematics are typically fit within about  $0.9\sigma$  per point, slightly better than required. This is due to the relatively low value used for the entropy smoothing, needed not to bias the range of allowed potentials by the imposed smoothing. The PN  $\chi^2$  values indicate that the PN data are consistent with all models.

The likelihood values for the models reported in Table 2 would formally allow us to exclude a large fraction of the halo potentials tested, using  $\Delta\mathcal{L} = 0.5$ . However, these likelihood differences depend to a significant degree on very few PNe in the wings of the LOSVDs. To assess this we have compared histograms of PN velocities with the LOSVDs of these models in cones along the major and minor axes. A  $\chi^2$  test shows that all model LOSVDs except for the model without dark halo are formally consistent with the PNe velocity histograms and associated Poisson errors. However, the low dark matter models show systematic deviations in form from the more flat-topped data histograms, which we judge significant for models A to C. Also, for these models the LOSVD  $\chi^2$  and the likelihood are correlated, which is not the case for the more massive halo models. On the basis of these findings we believe the likelihood results can probably be trusted for ruling out models A-C, but not for any of the more massive halo models. Thus we estimate that the range of circular velocities at  $5R_e$  consistent with the data is  $v_c(5R_e) \gtrsim 200 \text{ km s}^{-1}$ , with the best models having

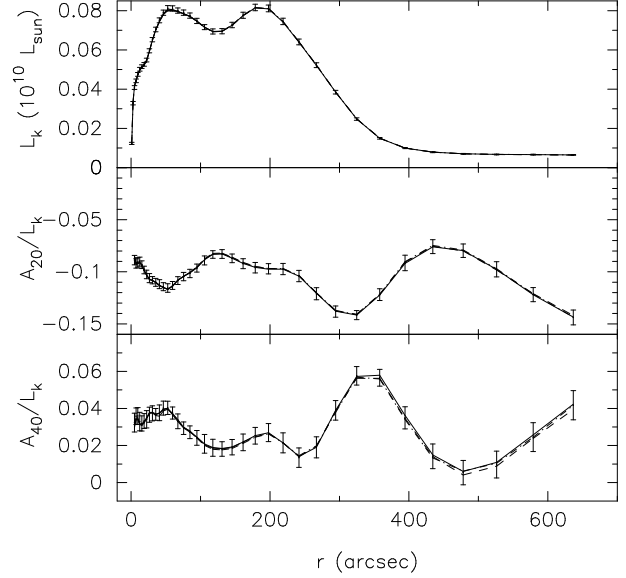


**Figure 16.** Comparison of the photometric constraints with the final models A (self-consistent, dashed), D (dotted), and G (full line). The points correspond to the target input data. From top to bottom: luminosity on radial shells profile  $L_k = \sqrt{4\pi}A_{00}$ , and normalized  $A_{20}$  and  $A_{40}$  profiles.

$v_c(5R_e) \simeq 250 \text{ km s}^{-1}$ . To reach more stringent constraints will require PN velocities at even larger radii.

Figures 16, 17, 18 present results from some of these models, comparing the stars-only model A and the three halo models D, G, and K to the data. Figure 16 shows the comparison of models A, D, G with the photometric constraints. The model lines match the target data points perfectly, in accordance with the very small  $\chi^2_{alm}/N_{alm}$  values in Table 1. Figure 17 compares the projected absorption line kinematics of the three models with our measurements and the BDI data. The fits are generally excellent. Along the major and minor axes one can see how the models have found compromises to deal with asymmetries of the data on both sides of the galaxy, and slight discrepancies between our and the BDI data, e.g., in the region around  $\pm 10''$  along the major axis. As for the isotropic rotator, the major axis higher order moments in Fig. 17 are even somewhat overfitted; see the discussion in Section 4.1.

Figure 18 compares the final A, D, G, and K models with the PNe kinematic constraints along the major axis (left) and minor axis (right); on each axis we show mean velocity (top) and velocity dispersion (bottom). The model curves in Fig. 18 and the  $\chi^2$  per data point values in Table 1 are computed for PN dataset PND1. There was no difference between these values and those obtained with PN dataset PND2 in all cases where we modelled both. The two additional lines in the panels of Fig. 18 show the mean velocities and velocity dispersions for the variants of models A, K obtained with the likelihood scheme for the PNe (see Section 3.5), computed by binning the particles in these models a posteriori in the same bins as for dataset PND1. While there is little difference for model K, the likelihood variant of model A fits the observed PN data points actually better than the original model A based on the PND1 data.

Overall, this figure illustrates that with increasing halo



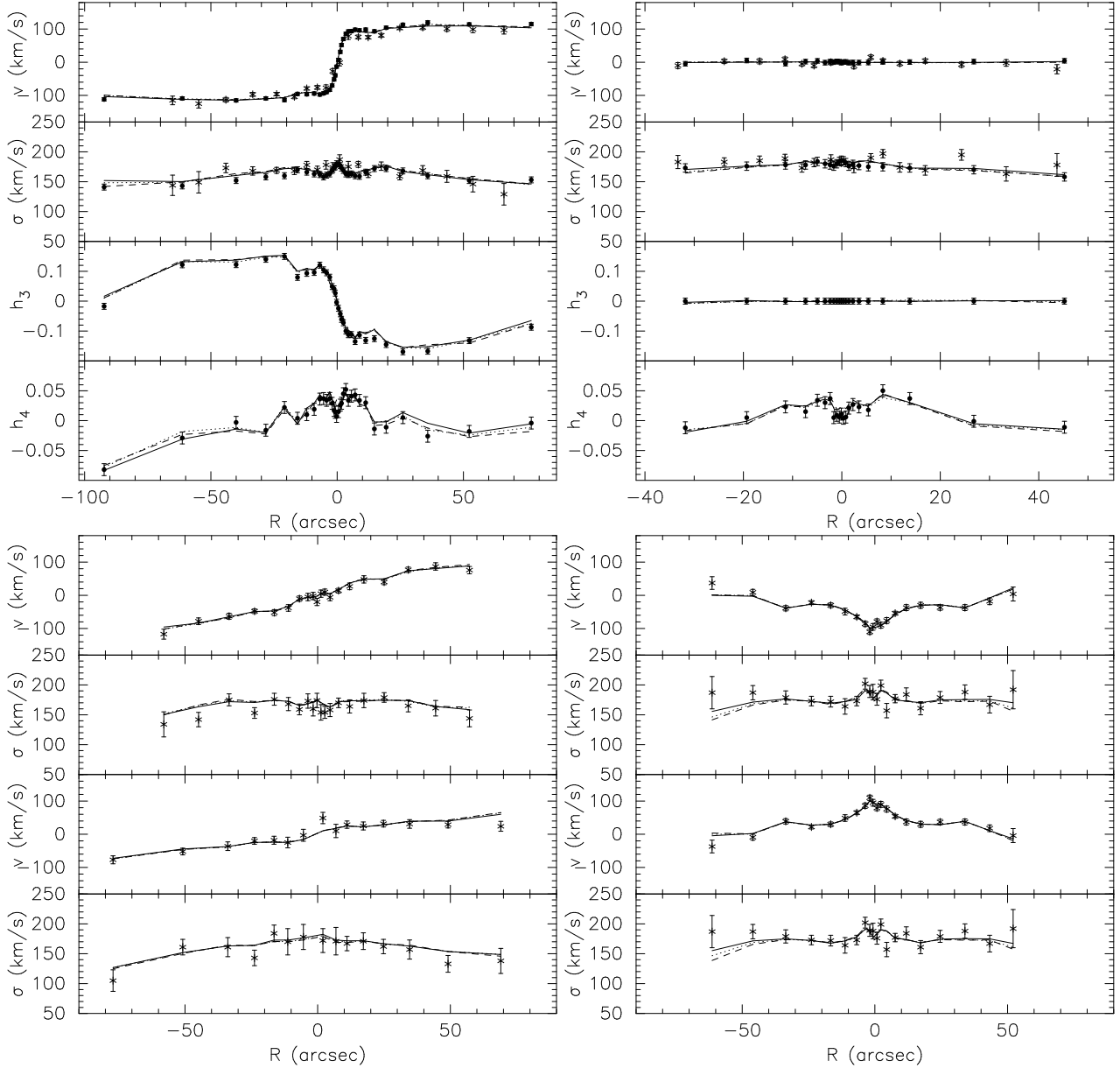


**Figure 17.** Comparison of models A, D, and G to the absorption line kinematic data along the major axis (top left), minor axis (top right), the slits parallel to the major axis (bottom left), and the slits parallel to the minor axis (bottom right). Full and starred data points show our new data and the BDI data, respectively. The model data points are averages over the same slit cells as the target data (see Fig. 5), and are connected by straight line segments. Linestyles for the models are the same as in Fig. 16.

mass the fit to the PNe kinematic data improves slightly. Models G and K bracket the best-fitting models to the binned data in Fig. 18. However, also model A without dark matter still has a  $\chi^2_{PN}/N_{PN}$  just below one, despite being systematically a little low in the minor axis dispersion plot. When we force the self-consistent model to improve the PN data fit at the expense of the slit kinematic data fit, the model starts to develop specific anisotropy features at the radii of the outer PN data. This suggests that with PN data extending to somewhat larger radii,  $\approx 400$  arcsec ( $R \approx 6R_e$ ), the model without dark halo might start to fail also for the binned data in Fig. 18, consistent with the likelihood and LOSVD results. In conclusion, a variety of dark halos with

$v_c(5R_e) \gtrsim 200 \text{ km s}^{-1}$  are consistent with all the kinematic data currently available for NGC 4697.

Finally, Figure 19 shows the internal kinematics of the particle models A, D, G, and K. The upper panels give  $\sigma_R$ ,  $\sigma_\phi$  and  $\sigma_z$ , followed by  $v_\phi$ . The last panel displays the anisotropy parameter  $\beta_\theta = 1 - \sigma_\theta^2/\sigma_r^2$ , which is zero for an isotropic rotator model. All quantities are given as averages over the models' equatorial plane. The more massive halo models become more radially anisotropic in the outer parts in terms of  $\sigma_R$  vs.  $\sigma_\phi$ , but  $\beta_\theta$  does not increase beyond model D because  $\sigma_R$  and  $\sigma_z$  increase in parallel while  $\sigma_\phi$  remains constant. Thus the additional kinetic energy that stars at large radii must have in these models, is hidden in

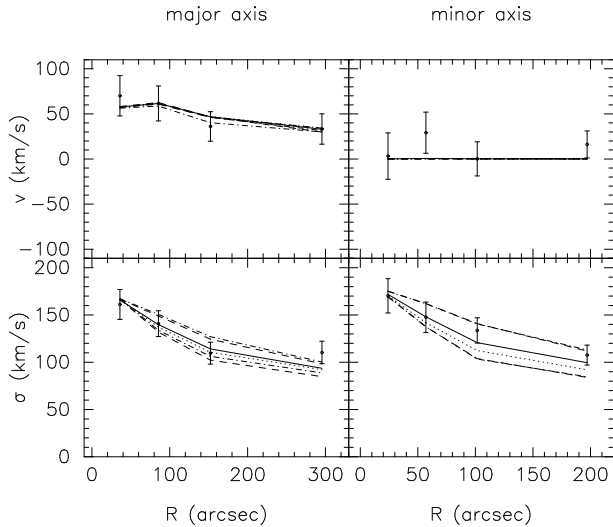


**Figure 18.** Comparison of the PNe velocity and velocity dispersion data (PND1, points) with models A, D, G, and K. Top left:  $v$  along the positive major axis. Top right: The same for the minor axis. Bottom left:  $\sigma$  along the positive major axis. Bottom right: The same but for the minor axis. Dashed, dotted, full, and upper dashed lines show models A, D, G, and K; the two dash-dotted lines show the variants of models A and K obtained with the likelihood scheme for the PNe.

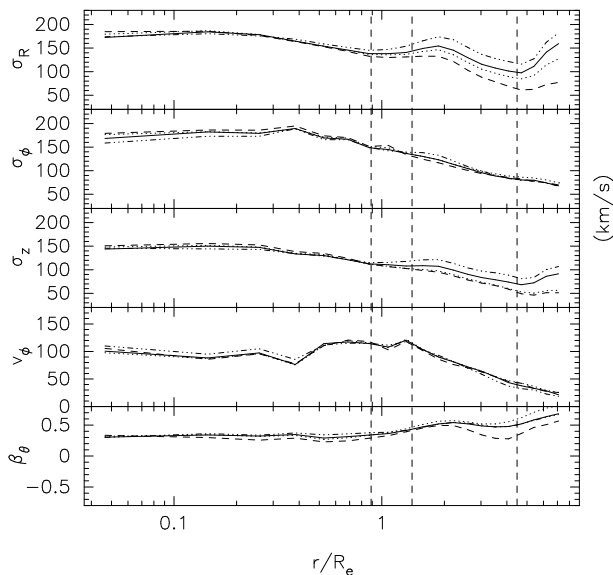


**Figure 19.** Internal velocity moments in the equatorial plane for models A, D, G, K (dashed, dotted, full, and dash-triple dotted lines, respectively). The vertical dashed lines indicate the radial extent of the minor axis slit data, major axis slit data, and PN data, from left to right.

the plane of the sky. Conversely, at small radii the velocity dispersions in models G-K are slightly lower, compensating for the larger radial velocities of halo stars along the line-of-sight to the center. These models have  $\beta \simeq 0.3$  at the center, which increases with radius and reaches  $\beta \simeq 0.5$  at  $\gtrsim 2R_e$ .

## 6 SUMMARY AND CONCLUSIONS

In this paper, we have presented new surface brightness measurements and long slit spectroscopic data for the E4 galaxy NGC 4697, and combined these data with existing long slit kinematics and discrete PNe position and velocity measurements to construct dynamical models for this galaxy. The combined data set runs from the center of the galaxy to about 4.5 effective radii.

For the first time, we have modelled such a dataset with the new and flexible  $\chi^2$ -made-to-measure ( $\chi^2$ M2M) particle code NMAGIC. We have extended NMAGIC to include seeing effects and have implemented an efficient method to estimate the mass-to-light ratio  $\Upsilon$ . Tests of this scheme using isotropic rotator input models have shown that the method recovers  $\Upsilon$  within a few percent both for self-consistent and dark matter dominated target galaxies. In addition, we have implemented a likelihood scheme which allows us to treat the PNe as discrete velocity measurements, so that no binning in velocities is needed. The modelling presented in this paper shows that the  $\chi^2$ M2M/NMAGIC particle method is now competitive with the familiar Schwarzschild method. In fact, it has already gone further in that the gravitational potential of the stars has been allowed to vary in the modelling, the mass-to-light ratio has been adapted on the fly, the stability of the models has been checked, and, in de Lorenzi et al. (2007), NMAGIC has been used to construct triaxial and rotating triaxial models.

Even though NMAGIC does not require any symmetry assumptions for the modelling, we have in this paper forced the method to generate axisymmetric particle models for NGC 4697. Both self-consistent models without dark matter, and models following a sequence of circular speed curves with increasing dark halo contributions have been investigated. The PN data have been used both binned on two different spatial grids, as well as with the new likelihood scheme, to make sure that the results are not biased by the way the PNe data are incorporated.

Our main astronomical result is that models with a variety of dark matter halos are consistent with all the data for NGC 4697, as long as the circular velocity  $v_c(5R_e) \gtrsim 200 \text{ km s}^{-1}$  at  $5R_e$ . These models include potentials with sufficiently massive halos to generate nearly flat circular rotation curves. These models fit all kinematic data with  $\chi^2/N < 1$ , including the PN LOSVDs. Models with no dark matter are not consistent with the PN LOSVDs, as judged from both the LOSVD histograms and their likelihood values. Amongst the acceptable models, the more massive dark halo models with  $v_c(5R_e) \simeq 250 \text{ km s}^{-1}$  tend to fit the data slightly better in the sense of lower  $\chi^2/N$ , for both the slit kinematics and the PN data, but these variations are small and not yet statistically significant. To further narrow down the range of acceptable dark matter models would require PN velocities at even larger radii than currently available, out to an estimated  $\simeq 6R_e$  from the center.

Our models differ from earlier studies performed by Méndez et al. (2001) in the sense that we generate axisymmetric models instead of spherical ones and that our models are flexible with regard to anisotropy. The best-fitting models are slightly radially anisotropic, with  $\beta \simeq 0.3$  at the center, increasing to  $\beta \simeq 0.5$  at  $\gtrsim 2R_e$ . This is consistent with the value given by Dekel et al. (2005) obtained from

merger simulations carried out within the  $\Lambda$ CDM cosmology framework.

## ACKNOWLEDGMENTS

We thank Lodovico Coccato for help with the data and the anonymous referee for comments that led to a better understanding of the effect of entropy on the models' smoothness. VPD is grateful for a Brooks Prize Fellowship while at the University of Washington. RHM would like to acknowledge support by the U.S. National Science Foundation under Grant 0307489.

## REFERENCES

- Arnaboldi M., Freeman K. C., Gerhard O., Matthias M., Kudritzki R. P., Méndez R. H., Capaccioli M., Ford H., 1998, *ApJ*, 507, 759
- Arnaboldi M., Freeman K. C., Méndez R. H., Capaccioli M., Ciardullo R., Ford H., Gerhard O., Hui X., Jacoby G. H., Kudritzki R. P., Quinn P. J., 1996, *ApJ*, 472, 145
- Awaki H., Mushotzky R., Tsuru T., Fabian A. C., Fukazawa Y., Loewenstein M., Makishima K., Matsumoto H., Matsushita K., Mihara T., Ohashi T., Ricker G. R., Serlemitsos P. J., Tsusaka Y., Yamazaki T., 1994, *PASJ*, 46, L65
- Bender R., Moellenhoff C., 1987, *A&A*, 177, 71
- Bender R., Saglia R., Gerhard O., 1994, *MNRAS*, 269, 785
- Binney J., Tremaine S., 1987, *Galactic Dynamics*. Princeton, NJ, Princeton University Press
- Binney J. J., Davies R. L., Illingworth G. D., 1990, *ApJ*, 361, 78
- Cappellari M., Bacon R., Bureau M., Damen M. C., Davies R. L., de Zeeuw P. T., Emsellem E., Falcón-Barroso J., Krajnović D., Kuntschner H., McDermid R. M., Peletier R. F., Sarzi M., van den Bosch R. C. E., van de Ven G., 2006, *MNRAS*, 366, 1126
- Carollo C. M., de Zeeuw P. T., van der Marel R. P., 1995, *MNRAS*, 276, 1131
- Carter D., 1987, *ApJ*, 312, 514
- de Blok W. J. G., Bosma A., McGaugh S., 2003, *MNRAS*, 340, 657
- de Lorenzi F., Debattista V. P., Gerhard O., Sambhus N., 2007, *MNRAS*, 376, 71
- Debattista V. P., Sellwood J. A., 2000, *ApJ*, 543, 704
- Dehnen W., 1993, *MNRAS*, 265, 250
- Dehnen W., Gerhard O. E., 1994, *MNRAS*, 268, 1019
- Dejonghe H., de Bruyne V., Vauterin P., Zeilinger W. W., 1996, *A&A*, 306, 363
- Dekel A., Stoehr F., Mamon G. A., Cox T. J., Novak G. S., Primack J. R., 2005, *Nature*, 437, 707
- Douglas N. G., Napolitano N. R., Romanowsky A. J., Coccato L., Kuijken K., Merrifield M. R., Arnaboldi M., Gerhard O., Freeman K. C., Merrett H. R., Noordermeer E., Capaccioli M., 2007, *ApJ*, 664, 257
- Fried J., Illingworth G., 1994, *AJ*, 107, 992
- Gebhardt K., Richstone D., Tremaine S., Lauer T. R., Bender R., Bower G., Dressler A., Faber S. M., Filippenko A. V., Green R., Grillmair C., Ho L. C., Kormendy J., Magorrian J., Pinkney J., 2003, *ApJ*, 583, 92
- Gerhard O., Jeske G., Saglia R. P., Bender R., 1998, *MNRAS*, 295, 197
- Gerhard O., Kronawitter A., Saglia R. P., Bender R., 2001, *AJ*, 121, 1936
- Gerhard O. E., 1993, *MNRAS*, 265, 213
- Gerhard O. E., Binney J. J., 1996, *MNRAS*, 279, 993
- Goudfrooij P., Hansen L., Jorgensen H. E., Norgaard-Nielsen H. U., de Jong T., van den Hoek L. B., 1994, *A&AS*, 104, 179
- Griffiths R. E., Casertano S., Im M., Ratnatunga K. U., 1996, *MNRAS*, 282, 1159
- Hernquist L., 1990, *ApJ*, 356, 359
- Hui X., Ford H. C., Freeman K. C., Dopita M. A., 1995, *ApJ*, 449, 592
- Humphrey P. J., Buote D. A., Gastaldello F., Zappacosta L., Bullock J. S., Brighenti F., Mathews W. G., 2006, *ApJ*, 646, 899
- Illingworth G. D., Schechter P. L., 1982, *ApJ*, 256, 481
- Irwin J. A., Sarazin C. L., Bregman J. N., 2000, *ApJ*, 544, 293
- Kalnajis A. J., 1977, *ApJ*, 212, 637
- Kochanek C. S., Rybicki G. B., 1996, *MNRAS*, 280, 1257
- Koprolin W., A. Zeilinger W., 2000, *A&AS*, 145, 71
- Kronawitter A., Saglia R. P., Gerhard O., Bender R., 2000, *A&AS*, 144, 53
- Loewenstein M., White III R. E., 1999, *ApJ*, 518, 50
- Lynden-Bell D., 1962, *MNRAS*, 123, 447
- Magorrian J., 1999, *MNRAS*, 302, 530
- Magorrian J., Binney J., 1994, *MNRAS*, 271, 949
- McGaugh S. S., de Blok W. J. G., Schombert J. M., Kuzio de Naray R., Kim J. H., 2007, *ApJ*, 659, 149
- Mehlert D., Saglia R., Bender R., Wegner G., 2000, *A&AS*, 141, 449
- Méndez R. H., Riffeser A., Kudritzki R.-P., Matthias M., Freeman K. C., Arnaboldi M., Capaccioli M., Gerhard O. E., 2001, *ApJ*, 563, 135
- Méndez R. H., Thomas D., Saglia R. P., Maraston C., Kudritzki R. P., Bender R., 2005, *ApJ*, 627, 767
- Moore B., Quinn T., Governato F., Stadel J., Lake G., 1999, *MNRAS*, 310, 1147
- Navarro J. F., Frenk C. S., White S. D. M., 1996, *ApJ*, 462, 563
- Peletier R. F., Davies R. L., Illingworth G. D., Davis L. E., Cawson M., 1990, *AJ*, 100, 1091
- Pinkney J., Gebhardt K., Bender R., Bower G., Dressler A., Faber S. M., Filippenko A. V., Green R., Ho L. C., Kormendy J., Lauer T. R., Magorrian J., Richstone D., Tremaine S., 2003, *ApJ*, 596, 903
- Pinkney J., Gebhardt K., Richstone D., Nuker Team 2000, *Bulletin of the American Astronomical Society*, 32, 1437
- Rix H.-W., de Zeeuw P. T., Cretton N., van der Marel R. P., Carollo C. M., 1997, *ApJ*, 488, 702
- Romanowsky A. J., Douglas N. G., Arnaboldi M., Kuijken K., Merrifield M. R., Napolitano N. R., Capaccioli M., Freeman K. C., 2003, *Science*, 301, 1696
- Romanowsky A. J., Kochanek C. S., 2001, *ApJ*, 553, 722
- Rusin D., Kochanek C. S., 2005, *ApJ*, 623, 666
- Rybicki G. B., 1987, in de Zeeuw P. T., ed., *IAU Symp. 127: Structure and Dynamics of Elliptical Galaxies* p. 397
- Sambhus N., Gerhard O., Méndez R. H., 2006, *AJ*, 131, 837

- Sansom A. E., Hibbard J. E., Schweizer F., 2000, *AJ*, 120, 1946
- Scorza C., Bender R., 1995, *A&A*, 293, 20
- Scorza C., Bender R., Winkelmann C., Capaccioli M., Macchetto D. F., 1998, *A&AS*, 131, 265
- Sellwood J. A., 2003, *ApJ*, 587, 638
- Syer D., Tremaine S., 1996, *MNRAS*, 282, 223
- Thomas J., Saglia R. P., Bender R., Thomas D., Gebhardt K., Magorrian J., Corsini E. M., Wegner G., 2005, *MNRAS*, 360, 1355
- Thomas J., Saglia R. P., Bender R., Thomas D., Gebhardt K., Magorrian J., Corsini E. M., Wegner G., 2007, *MNRAS*, in press
- Tonry J. L., Dressler A., Blakeslee J. P., Ajhar E. A., Fletcher A. B., Luppino G. A., Metzger M. R., Moore C. B., 2001, *ApJ*, 546, 681
- Tremblay B., Merritt D., Williams T. B., 1995, *ApJ*, 443, L5
- Treu T., Koopmans L. V. E., 2004, *ApJ*, 611, 739
- van der Marel R. P., Franx M., 1993, *ApJ*, 407, 525
- van der Marel R. P., Rix H.-W., Carter D., Franx M., White S. D. M., de Zeeuw P. T., 1994, *MNRAS*, 268, 521

## **APPENDIX A: PHOTOMETRIC AND KINEMATIC DATA**

Table A: Photometric parameters of NGC 4697

a	$\mu_R^a$	e	PA	$\Delta x_c$	$\Delta y_c$	Err. <sup>b</sup>	$a_3/a$	$b_3/a$	$a_4/a$	$b_4/a$	$a_6/a$	$b_6/a$	Err. <sup>c</sup>
[arcsec]	[mag arcsec <sup>-2</sup> ]		[°]	[arcsec]	[arcsec]	[arcsec]	×100	×100	×100	×100	×100	×100	
1.013 ± 0.013	15.515± 0.006	0.246± 0.013	65.8± 2.0	-0.012	0.007	0.009	0.110	4.380	2.750	0.380	0.260	-0.210	0.162
1.201 ± 0.014	15.635± 0.008	0.247± 0.013	67.0± 2.0	0.000	0.000	0.010	0.430	4.850	2.750	-0.490	-0.180	0.160	0.123
1.359 ± 0.020	15.753± 0.007	0.212± 0.017	67.6± 2.9	0.019	0.019	0.014	0.620	6.790	3.580	-0.610	-0.080	-0.160	0.080
1.517 ± 0.029	15.847± 0.008	0.157± 0.023	68.0± 4.9	0.045	0.071	0.020	0.520	9.620	3.570	0.240	1.030	-1.090	0.151
1.739 ± 0.028	15.929± 0.008	0.151± 0.019	66.7± 4.3	0.069	0.129	0.020	-0.660	8.320	0.440	0.840	1.630	-0.200	0.206
2.023 ± 0.025	16.030± 0.006	0.188± 0.014	66.4± 2.6	0.083	0.162	0.018	-0.650	6.000	-1.680	0.440	0.100	0.160	0.154
2.365 ± 0.021	16.134± 0.005	0.242± 0.009	66.0± 1.5	0.095	0.190	0.015	-0.540	3.580	-2.690	0.130	-1.570	0.300	0.112
2.759 ± 0.017	16.233± 0.004	0.297± 0.006	65.6± 0.8	0.100	0.212	0.012	-0.320	1.540	-2.220	-0.270	-2.310	-0.070	0.114
3.235 ± 0.009	16.333± 0.003	0.358± 0.003	65.7± 0.3	0.109	0.221	0.007	-0.340	0.430	-0.600	-0.120	-1.430	-0.010	0.158
3.747 ± 0.007	16.436± 0.002	0.406± 0.001	65.8± 0.2	0.112	0.226	0.005	-0.260	-0.070	1.420	-0.070	0.100	-0.030	0.023
4.138 ± 0.008	16.537± 0.002	0.417± 0.002	65.8± 0.2	0.114	0.228	0.006	-0.200	-0.140	1.650	-0.060	0.140	-0.030	0.020
4.525 ± 0.008	16.637± 0.002	0.422± 0.001	65.8± 0.2	0.119	0.228	0.006	-0.250	-0.110	1.600	-0.030	0.130	0.080	0.023
4.932 ± 0.009	16.737± 0.002	0.425± 0.001	65.8± 0.2	0.126	0.228	0.006	-0.360	-0.060	1.590	-0.050	0.110	0.080	0.025
5.363 ± 0.009	16.837± 0.002	0.426± 0.001	65.9± 0.2	0.126	0.228	0.006	-0.290	-0.000	1.560	-0.050	0.040	0.150	0.027
5.835 ± 0.009	16.937± 0.002	0.428± 0.001	65.8± 0.2	0.133	0.226	0.006	-0.210	0.010	1.570	-0.030	-0.000	0.130	0.034
6.345 ± 0.010	17.037± 0.002	0.430± 0.001	65.9± 0.1	0.133	0.224	0.007	-0.070	0.080	1.590	-0.020	-0.010	0.070	0.034
6.881 ± 0.011	17.137± 0.002	0.431± 0.001	66.1± 0.1	0.138	0.217	0.007	0.120	0.130	1.620	-0.070	-0.110	-0.020	0.029
7.444 ± 0.011	17.237± 0.001	0.431± 0.001	66.2± 0.1	0.145	0.210	0.008	0.210	0.040	1.520	-0.190	-0.010	-0.110	0.039
8.056 ± 0.012	17.337± 0.001	0.430± 0.001	66.2± 0.1	0.138	0.210	0.008	0.210	0.000	1.530	-0.190	0.120	-0.070	0.039
8.706 ± 0.014	17.437± 0.001	0.428± 0.001	66.1± 0.2	0.138	0.198	0.010	0.160	0.160	1.720	-0.110	0.210	-0.090	0.038
9.398 ± 0.016	17.536± 0.001	0.427± 0.001	66.1± 0.2	0.138	0.193	0.011	0.150	0.150	1.720	0.100	0.300	-0.010	0.059
10.136 ± 0.016	17.635± 0.001	0.424± 0.001	66.1± 0.2	0.140	0.186	0.011	0.160	0.120	1.610	0.060	0.320	0.000	0.044
10.900 ± 0.015	17.736± 0.001	0.419± 0.001	66.2± 0.1	0.138	0.176	0.011	0.150	0.090	1.420	0.060	0.260	0.090	0.039
11.706 ± 0.015	17.837± 0.001	0.414± 0.001	66.0± 0.1	0.131	0.174	0.011	0.110	0.110	1.360	0.080	0.210	0.080	0.031
12.598 ± 0.017	17.937± 0.001	0.411± 0.001	66.0± 0.1	0.112	0.181	0.012	0.170	0.130	1.400	0.020	0.250	-0.040	0.052
13.531 ± 0.018	18.036± 0.001	0.407± 0.001	66.0± 0.1	0.117	0.176	0.013	0.110	0.080	1.360	-0.060	0.200	-0.090	0.039
14.530 ± 0.018	18.136± 0.001	0.405± 0.001	66.0± 0.1	0.119	0.174	0.013	0.010	0.090	1.320	-0.070	0.160	-0.100	0.028
15.595 ± 0.022	18.236± 0.001	0.403± 0.001	66.1± 0.1	0.121	0.178	0.016	-0.070	0.100	1.420	-0.090	0.250	-0.190	0.030
16.761 ± 0.027	18.335± 0.001	0.402± 0.001	66.2± 0.2	0.107	0.188	0.019	-0.130	0.160	1.430	-0.110	0.370	-0.320	0.050
18.038 ± 0.029	18.435± 0.001	0.405± 0.001	66.2± 0.2	0.105	0.193	0.021	-0.130	0.140	1.500	-0.110	0.470	-0.260	0.039
19.477 ± 0.034	18.537± 0.001	0.413± 0.001	66.4± 0.2	0.088	0.193	0.024	-0.050	0.140	1.660	-0.020	0.490	-0.120	0.034
20.955 ± 0.049	18.637± 0.001	0.419± 0.002	66.1± 0.2	0.157	0.181	0.035	-0.100	-0.140	1.890	-0.300	0.670	-0.350	0.130
22.554 ± 0.074	18.735± 0.001	0.425± 0.003	65.8± 0.3	0.248	0.162	0.053	-0.230	-0.350	2.070	-0.520	0.790	-0.540	0.270
24.352 ± 0.078	18.835± 0.001	0.433± 0.003	65.8± 0.3	0.228	0.186	0.055	-0.150	-0.220	2.020	-0.340	0.540	-0.380	0.254
26.452 ± 0.056	18.936± 0.001	0.446± 0.002	65.9± 0.2	0.093	0.264	0.040	0.070	-0.000	2.070	0.020	0.400	-0.050	0.070
28.543 ± 0.057	19.036± 0.001	0.453± 0.001	66.0± 0.2	0.150	0.274	0.040	0.030	-0.040	1.940	0.080	0.510	-0.090	0.077
30.687 ± 0.060	19.135± 0.001	0.458± 0.001	65.9± 0.2	0.147	0.290	0.042	0.020	-0.050	1.870	-0.040	0.650	-0.150	0.059
32.840 ± 0.060	19.236± 0.001	0.459± 0.001	65.9± 0.2	0.124	0.302	0.042	-0.010	-0.070	1.720	-0.140	0.760	-0.120	0.044
35.061 ± 0.062	19.336± 0.001	0.459± 0.001	65.9± 0.2	0.088	0.312	0.044	-0.020	-0.040	1.550	-0.210	0.880	-0.090	0.045
37.385 ± 0.059	19.435± 0.001	0.458± 0.001	66.1± 0.1	0.102	0.314	0.042	0.030	-0.060	1.280	-0.100	0.810	-0.140	0.066
39.678 ± 0.060	19.536± 0.001	0.455± 0.001	66.1± 0.1	0.078	0.326	0.042	-0.080	0.010	1.290	-0.080	0.830	0.020	0.050
42.182 ± 0.066	19.635± 0.001	0.453± 0.001	66.3± 0.1	0.074	0.343	0.046	0.070	-0.060	1.190	-0.070	0.860	0.020	0.071
44.663 ± 0.072	19.734± 0.001	0.448± 0.001	66.3± 0.2	0.028	0.359	0.051	0.140	-0.040	1.250	-0.070	0.940	-0.000	0.062
47.108 ± 0.073	19.834± 0.001	0.442± 0.001	66.3± 0.1	0.010	0.402	0.052	0.020	-0.100	1.190	-0.100	0.950	-0.120	0.074
49.534 ± 0.078	19.934± 0.001	0.436± 0.001	66.3± 0.2	-0.088	0.409	0.055	-0.030	0.010	1.210	-0.240	1.000	-0.110	0.045

a	$\mu_R^a$	e	PA	$\Delta x_c$	$\Delta y_c$	Err. <sup>b</sup>	$a_3/a$	$b_3/a$	$a_4/a$	$b_4/a$	$a_6/a$	$b_6/a$	Err. <sup>c</sup>
[arcsec]	[mag arcsec <sup>-2</sup> ]		[°]	[arcsec]	[arcsec]	[arcsec]	×100	×100	×100	×100	×100	×100	
51.950 ± 0.083	20.036± 0.001	0.428± 0.001	66.4± 0.2	-0.119	0.402	0.059	...	...	...	...	...	...	0.045
54.308 ± 0.087	20.135± 0.001	0.417± 0.001	66.2± 0.2	-0.098	0.459	0.062	-0.040	-0.040	1.060	-0.160	1.090	0.030	0.062
56.753 ± 0.092	20.235± 0.001	0.409± 0.001	66.5± 0.2	-0.167	0.424	0.065	-0.020	-0.110	0.790	-0.290	1.130	-0.020	0.065
59.253 ± 0.092	20.336± 0.001	0.399± 0.001	66.6± 0.2	-0.198	0.452	0.065	...	...	...	...	...	...	0.065
62.028 ± 0.092	20.436± 0.001	0.393± 0.001	66.6± 0.2	-0.298	0.502	0.065	-0.010	0.000	0.700	-0.240	1.150	-0.130	0.059
64.741 ± 0.082	20.536± 0.001	0.385± 0.001	66.6± 0.1	-0.345	0.505	0.058	-0.050	0.040	0.570	-0.160	0.960	-0.100	0.068
67.520 ± 0.078	20.635± 0.001	0.379± 0.001	66.5± 0.1	-0.205	0.476	0.055	-0.090	0.050	0.440	-0.190	0.990	0.010	0.048
70.445 ± 0.085	20.734± 0.001	0.372± 0.001	66.5± 0.1	-0.219	0.438	0.060	-0.140	0.030	0.360	-0.110	0.920	-0.090	0.064
73.422 ± 0.090	20.834± 0.001	0.364± 0.001	66.3± 0.1	-0.279	0.567	0.064	-0.140	-0.110	0.140	-0.170	0.850	-0.040	0.078
76.678 ± 0.085	20.936± 0.001	0.360± 0.001	66.4± 0.1	-0.140	0.583	0.060	...	...	...	...	...	...	0.078
80.086 ± 0.093	21.037± 0.001	0.354± 0.001	66.3± 0.1	-0.050	0.497	0.066	...	...	...	...	...	...	0.078
83.687 ± 0.109	21.138± 0.001	0.351± 0.001	66.4± 0.2	-0.228	0.436	0.077	-0.010	-0.080	0.010	-0.350	0.750	-0.060	0.094
87.231 ± 0.101	21.239± 0.001	0.344± 0.001	66.7± 0.1	-0.502	0.738	0.071	...	...	...	...	...	...	0.094
90.680 ± 0.120	21.339± 0.001	0.336± 0.001	66.6± 0.2	-0.398	0.769	0.085	...	...	...	...	...	...	0.094
94.336 ± 0.135	21.439± 0.001	0.329± 0.001	66.4± 0.2	-0.445	0.992	0.096	...	...	...	...	...	...	0.094
98.111 ± 0.165	21.538± 0.001	0.321± 0.002	66.3± 0.2	-0.457	1.004	0.117	...	...	...	...	...	...	0.094
101.661 ± 0.232	21.637± 0.001	0.311± 0.002	66.6± 0.3	-0.509	1.214	0.164	0.140	-0.240	-0.560	-0.110	0.640	0.340	0.200
105.981 ± 0.288	21.737± 0.001	0.309± 0.003	66.6± 0.4	-0.347	1.197	0.203	0.020	-0.200	-0.440	-0.260	0.540	0.340	0.210
111.325 ± 0.162	21.841± 0.001	0.312± 0.001	66.4± 0.2	-0.319	1.230	0.115	...	...	...	...	...	...	0.210
116.502 ± 0.166	21.944± 0.001	0.313± 0.001	66.3± 0.2	-0.664	1.511	0.117	0.270	-0.430	0.000	-0.450	0.740	-0.040	0.092
121.793 ± 0.201	22.043± 0.001	0.313± 0.002	66.1± 0.2	-0.652	1.433	0.142	...	...	...	...	...	...	0.092
127.455 ± 0.218	22.138± 0.001	0.313± 0.002	65.8± 0.2	-1.119	1.668	0.154	0.370	-0.440	0.260	-0.410	0.710	0.070	0.099
133.917 ± 0.324	22.234± 0.001	0.318± 0.002	65.7± 0.3	-1.509	2.154	0.229	0.420	-0.440	0.370	-0.480	0.970	0.290	0.170
139.843 ± 0.460	22.331± 0.001	0.314± 0.003	65.7± 0.4	-1.775	1.725	0.325	0.430	-0.340	0.400	-0.400	0.620	0.720	0.265
147.198 ± 0.536	22.430± 0.001	0.320± 0.003	64.8± 0.5	-2.335	1.937	0.379	...	...	...	...	...	...	0.265
155.523 ± 0.400	22.533± 0.001	0.326± 0.002	64.8± 0.3	-2.535	2.537	0.283	...	...	...	...	...	...	0.265
163.016 ± 0.359	22.633± 0.001	0.329± 0.002	64.2± 0.3	-2.982	2.651	0.254	...	...	...	...	...	...	0.265
170.075 ± 0.429	22.728± 0.001	0.329± 0.002	64.1± 0.3	-3.165	2.720	0.304	...	...	...	...	...	...	0.265
177.623 ± 0.365	22.827± 0.001	0.328± 0.002	63.2± 0.2	-3.611	2.977	0.258	0.160	-0.570	0.320	-0.470	0.440	-0.080	0.163
185.102 ± 0.334	22.934± 0.001	0.325± 0.002	62.8± 0.2	-4.251	3.075	0.237	...	...	...	...	...	...	0.163
190.987 ± 0.358	23.036± 0.001	0.320± 0.002	63.0± 0.2	-4.284	2.625	0.253	0.040	-0.670	-0.350	-0.140	0.320	-0.070	0.153
196.718 ± 0.432	23.132± 0.001	0.312± 0.002	62.8± 0.3	-4.146	2.013	0.305	0.070	-0.470	-0.350	0.330	0.260	0.220	0.200
202.089 ± 0.559	23.227± 0.001	0.303± 0.003	62.5± 0.4	-3.715	1.787	0.395	...	...	...	...	...	...	0.200
207.354 ± 0.675	23.323± 0.001	0.294± 0.003	62.2± 0.5	-3.703	1.692	0.478	...	...	...	...	...	...	0.200
212.802 ± 0.787	23.421± 0.001	0.290± 0.004	62.1± 0.5	-4.401	1.973	0.556	...	...	...	...	...	...	0.200
217.940 ± 0.851	23.521± 0.001	0.277± 0.004	62.0± 0.6	-5.084	2.106	0.602	...	...	...	...	...	...	0.200
222.191 ± 0.996	23.613± 0.001	0.266± 0.005	61.8± 0.7	-5.386	1.642	0.704	...	...	...	...	...	...	0.200
226.618 ± 1.524	23.707± 0.001	0.258± 0.007	62.0± 1.1	-5.745	1.259	1.078	...	...	...	...	...	...	0.200
233.406 ± 0.749	23.815± 0.001	0.260± 0.003	61.2± 0.5	-5.653	1.309	0.529	...	...	...	...	...	...	0.200
238.734 ± 0.519	23.925± 0.001	0.247± 0.002	60.9± 0.4	-7.590	1.397	0.367	...	...	...	...	...	...	0.200
243.821 ± 0.590	24.020± 0.001	0.246± 0.003	60.2± 0.4	-7.878	1.488	0.417	...	...	...	...	...	...	0.200
247.975 ± 0.827	24.104± 0.001	0.240± 0.004	59.6± 0.6	-7.811	1.447	0.585	...	...	...	...	...	...	0.200
253.321 ± 0.972	24.189± 0.001	0.245± 0.004	59.4± 0.6	-7.540	1.035	0.687	...	...	...	...	...	...	0.200

Dark matter content and internal dynamics of NGC 4697

<sup>a</sup> Statistical errors not including systematics due to photometric calibration and sky subtraction

<sup>b</sup> Error on the center coordinates from the residual rms of the ellipse fit to the isophotes: Err=rms(fit)/ $\sqrt{N}$  with  $N \leq 128$  the number of fitted points of the isophotes.

<sup>c</sup> Error of Fourier coefficients defined as Err= $\sqrt{\frac{\sum_{i=10}^{N/2} (a_i^2+b_i^2)}{N/2-10}} \times \frac{100}{a}$ .

**Table A1.** The kinematics of NGC 4697 along the major axis (P.A.=66°). Positive radii are to the north-east.

R (")	V (km/s)	dV (km/s)	$\sigma$ (km/s)	$d\sigma$ (km/s)	$h_3$	$dh_3$	$h_4$	$dh_4$
0.38	-13.2	0.4	180.0	0.4	-0.004	0.002	0.007	0.002
0.97	-39.5	0.2	175.3	0.4	0.027	0.002	0.014	0.002
1.57	-51.8	0.2	174.4	0.4	0.041	0.002	0.017	0.002
2.27	-70.1	0.3	169.4	0.4	0.049	0.002	0.029	0.002
3.16	-83.1	0.3	163.4	0.4	0.08	0.002	0.037	0.002
4.26	-89.9	0.3	160.6	0.4	0.095	0.002	0.034	0.002
5.55	-93.8	0.4	157.9	0.5	0.105	0.003	0.037	0.003
7.14	-97.3	0.4	162.3	0.5	0.12	0.002	0.036	0.002
9.22	-94.2	0.4	163.3	0.6	0.096	0.002	0.019	0.003
12.00	-96.6	0.4	166.3	0.5	0.093	0.002	0.010	0.002
15.67	-95.5	0.4	170.5	0.6	0.080	0.002	0.004	0.003
20.63	-114.1	0.6	160.3	0.8	0.150	0.003	0.022	0.004
27.62	-109.1	0.6	157.8	0.8	0.140	0.003	-0.016	0.004
38.07	-115.1	0.7	151.9	1.0	0.122	0.004	-0.003	0.005
58.05	-108.6	1.0	143.2	1.4	0.122	0.006	-0.029	0.007
92.52	-111.5	2.9	140.9	3.7	-0.017	0.020	-0.082	0.015
-0.22	7.0	0.4	179.6	0.4	-0.024	0.002	0.015	0.002
-0.81	31.3	0.3	177.0	0.4	-0.042	0.002	0.026	0.001
-1.41	51.9	0.3	173.3	0.4	-0.061	0.002	0.029	0.001
-2.11	70.1	0.3	169.0	0.5	-0.072	0.002	0.045	0.002
-3.00	85.6	0.3	163.4	0.5	-0.100	0.002	0.052	0.002
-4.00	92.8	0.3	161.8	0.3	-0.112	0.001	0.034	0.002
-5.19	93.6	0.3	162.7	0.3	-0.112	0.001	0.041	0.002
-6.69	98.0	0.3	160.3	0.3	-0.135	0.001	0.043	0.002
-8.57	96.0	0.3	159.1	0.3	-0.114	0.001	0.034	0.002
-11.05	98.3	0.3	165.8	0.3	-0.131	0.001	0.030	0.002
-14.32	93.2	0.3	172.2	0.3	-0.126	0.001	-0.014	0.002
-18.79	103.9	0.3	172.1	0.3	-0.145	0.001	-0.011	0.002
-24.99	112.6	0.4	168.1	0.3	-0.170	0.002	0.005	0.002
-34	120.1	0.5	160.0	0.5	-0.168	0.002	-0.026	0.003
-48.87	113.7	0.7	152.5	0.6	-0.132	0.004	-0.018	0.004
-76.65	115.2	1.9	153.1	2.1	-0.087	0.012	-0.004	0.010

**Table A2.** The kinematics of NGC 4697 along the minor axis (P.A.=156°). Positive radii are to the south-east.

R (")	V (km/s)	dV (km/s)	$\sigma$ (km/s)	$d\sigma$ (km/s)	$h_3$	$dh_3$	$h_4$	$dh_4$
0.09	-1.3	0.2	186.3	0.2	-0.014	0.001	0.011	0.001
0.49	1.6	0.3	183.7	0.3	-0.001	0.001	0.006	0.001
1.00	2.3	0.1	179.8	0.1	-0.013	0.005	0.009	0.001
1.58	0.3	0.3	176.4	0.3	-0.007	0.001	0.005	0.001
2.27	1.6	0.3	177.9	0.3	0.001	0.001	0.037	0.001
3.25	-1.3	0.2	180.4	0.2	-0.001	0.001	0.030	0.001
4.73	4.1	0.3	184.3	0.3	-0.006	0.001	0.034	0.001
6.98	1.9	0.3	178.1	0.3	-0.019	0.001	0.015	0.001
10.66	-4.2	0.5	177.6	0.5	-0.022	0.002	0.023	0.002
17.37	5.2	0.7	175.9	0.7	-0.007	0.003	0.005	0.002
31.77	-4.6	1.4	173.2	1.4	-0.005	0.006	-0.012	0.005
-0.31	0.6	0.2	185.0	0.2	0.020	0.001	0.004	0.001
-0.80	1.0	0.1	181.9	0.1	0.018	0.005	0.006	0.001
-1.40	-1.4	0.2	176.5	0.2	0.018	0.001	0.021	0.001
-2.18	-0.8	0.3	178.9	0.3	0.013	0.001	0.027	0.001
-3.36	-1.9	0.3	176.7	0.3	-0.004	0.001	0.023	0.001
-5.13	-0.8	0.3	175.0	0.3	0.020	0.001	0.018	0.001
-7.95	1.0	0.4	175.2	0.5	0.020	0.002	0.050	0.002
-12.74	0.6	0.6	173.2	0.7	0.015	0.003	0.037	0.003
-22.55	1.9	0.9	169.7	1.0	0.017	0.004	-0.001	0.003
-49.42	4.4	2.1	158.1	2.3	0.001	0.010	-0.011	0.007



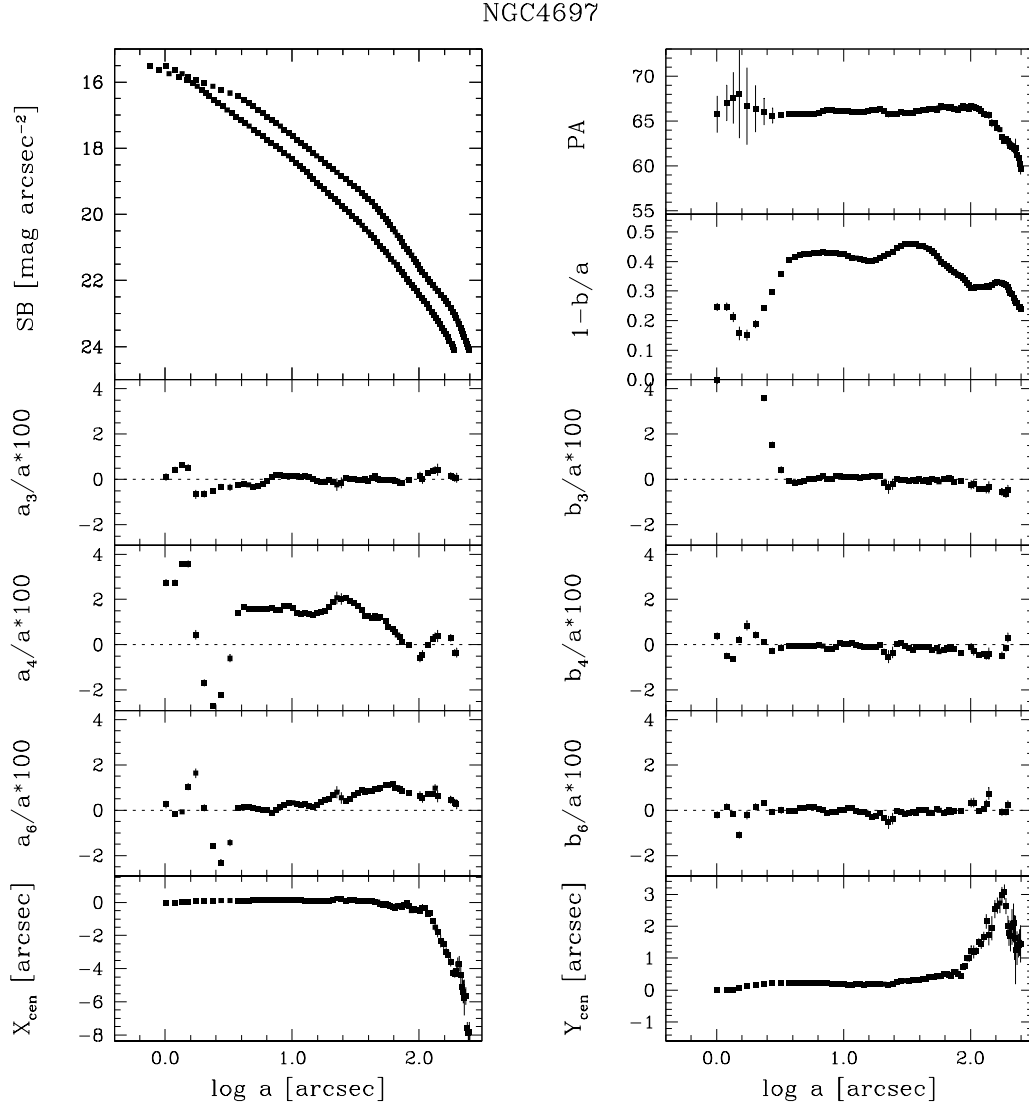


**Figure A1.** Isophotal parameters of NGC 4697 as a function of the logarithm of the semi-major axis distance in arcsec. The radial profiles of the R-band surface brightness, third, fourth, and sixth cosine Fourier coefficients ( $a_3$ ,  $a_4$ , and  $a_6$ ), and  $x$ -coordinate of the center  $X_{cen}$  are plotted in the left panels (from top to bottom). The surface brightness is shown along the major (upper profile) and minor axis (lower profile). The radial profiles of the position angle (PA), ellipticity ( $1 - b/a$ ), third fourth, and sixth sine Fourier coefficients ( $b_3$ ,  $b_4$ , and  $b_6$ ), and  $y$ -coordinate of the center ( $Y_{cen}$ ) are plotted in the right panels (from top to bottom).